Journal of Geophysical Research: Atmospheres

RESEARCH ARTICLE
10.1029/2018JD028779

Special Section:
Deep Convective Clouds and Chemistry 2012 Studies (DC3)

Key Points:
- Subgrid-scale convective transport was more significant relative to that at grid scale in a supercell case than in a MCS case
- Subgrid contribution was ~90% at the beginning of the storm and decreased to ~30% (17%) for the 36-km (12-km) domain 4 hr later
- Subgrid convective transport in chemical models needs to be consistent with the cloud parameterization in the driving meteorological model

Correspondence to:
Y. Li,
liyunyao@terpmail.umd.edu

Citation:
Li, Y., Pickering, K. E., Barth, M. C., Bela, M. M., Cummings, K. A., & Allen, D. J. (2018). Evaluation of parameterized convective transport of trace gases in simulation of storms observed during the DC3 field campaign. *Journal of Geophysical Research: Atmospheres*, *123*, 11,238–11,261. https://doi.org/10.1029/2018JD028779

Received 7 APR 2018
Accepted 11 SEP 2018
Accepted article online 14 SEP 2018
Published online 2 OCT 2018

©2018. American Geophysical Union. All Rights Reserved.

Evaluation of Parameterized Convective Transport of Trace Gases in Simulation of Storms Observed During the DC3 Field Campaign

Y. Li[1], **K. E. Pickering**[1], **M. C. Barth**[2], **M. M. Bela**[3], **K. A. Cummings**[4], **and D. J. Allen**[1]

[1]Department of Atmospheric and Oceanic Sciences, University of Maryland, College Park, MD, USA, [2]National Center for Atmospheric Research, Boulder, CO, USA, [3]University of Colorado Cooperative Institute for Research in Environmental Sciences (CIRES) at the NOAA Earth System Research Laboratory (ESRL) Chemical Sciences Division, Boulder, CO, USA, [4]Kennedy Space Center, National Aeronautics and Space Administration (NASA), FL, USA

Abstract Deep convective transport of surface moisture and pollution from the planetary boundary layer to the upper troposphere and lower stratosphere affects the radiation budget and climate. This study uses cloud-parameterized Weather Research and Forecasting model coupled with Chemistry simulations to analyze the subgrid deep convective transport of CO at 12- and 36-km horizontal resolution in supercell and mesoscale convective systems observed during the 2012 Deep Convective Clouds and Chemistry field campaign and compares the simulation results with aircraft measurements and cloud-resolved simulations. The best Weather Research and Forecasting simulation of these storms was obtained with the use of the Grell-Freitas convective scheme. The default Weather Research and Forecasting model coupled with Chemistry subgrid convective transport scheme was replaced with a scheme to compute convective transport within the Grell-Freitas subgrid cumulus parameterization, which resulted in improved transport simulations. We examined the CO tendencies due to subgrid- and grid-scale convective transport. Results showed that the subgrid convective transport started earlier than the grid-scale convective transport. The subgrid-scale convective transport reached its maximum during the hour prior to the formation of the grid-scale constant-altitude detrainment layer. After that, both the subgrid- and grid-scale convective transport began to decrease. The subgrid-scale convective transport played a more significant role in the supercell case than the mesoscale convective system case. Subgrid contribution reached ~90% at the beginning of the storm and decreased to ~30% (17%) for the 36-km (12-km) domain 4 hr later.

1. Introduction

Deep convection is a major redistributor of surface moisture and pollution from the planetary boundary layer (PBL) to the upper troposphere and lower stratosphere (Chatfield & Crutzen, 1984; Dickerson et al., 1987). It can take only a few minutes to an hour to transport an air parcel from the surface to the UT (Skamarock et al., 2000). Measurements from field campaigns (Apel et al., 2015; Bertram et al., 2007; Dickerson et al., 1987; Homeyer et al., 2014; Jung et al., 2005; Pickering et al., 1988, 1996, 2001; Scala et al., 1990; Stenchikov et al., 1996; Thompson et al., 1994; Wang et al., 1996) and satellites (Halland et al., 2009; Jensen et al., 2015; Levizzani & Setvák, 1996; Livesey et al., 2013; Setvak & Doswell, 1991) have demonstrated that deep convective transport strongly affects the moisture distribution and chemical composition of the upper troposphere and lower stratosphere.

The radiation budget and climate are affected by the transport of surface moisture and pollution in deep convection. The transport of local air pollutants from PBL to the free troposphere may transform local air pollution into regional or global atmospheric chemistry issues (Kong & Qin, 1993, 1994a; Lyons et al., 1986). Vertical transport of surface ozone and ozone precursor gases substantially increases the production rate of ozone in cloud outflow where the lifetime of ozone is longer compared to the PBL region, which significantly affects the Earth's radiation budget (Pickering et al., 1990; Pickering, Thompson, Scala, Tao, Dickerson, et al., 1992; Pickering, Thompson, Scala, Tao, & Simpson, 1992). Furthermore, the injection of PBL moisture into the stratosphere by deep convection enhances the concentration of water vapor in the lower stratosphere and is one of the causes for lower stratosphere water vapor variability (Homeyer et al., 2014). According to Solomon et al. (2010), stratospheric water vapor is a key driver for decadal global surface climate change.

Deep convective transport is a complex mechanism. Previous studies demonstrated that large-scale conditions (Pickering et al., 1988), PBL conditions (Stenchikov et al., 1996), storm vertical velocity (Pickering, Scala, et al., 1992), storm propagation speed (Wang et al., 1996), storm types (Bigelbach et al., 2014; Kong & Qin, 1994b), and inflow structure (Mullendore et al., 2005; Scala et al., 1990; Skamarock et al., 2000) each play an important role in the transport.

Model simulations at both cloud-parameterized and cloud-resolved resolutions are often used in deep convective transport studies. Barth et al. (2012) utilized the Weather Research and Forecasting model coupled with Chemistry (WRF-Chem; Fast et al., 2006; Grell et al., 2005; Peckham et al., 2011) to study the convective transport and chemistry associated with the early stages of the North American Monsoon, which was the first time WRF-Chem was applied at high resolution (4 km) over the entire continental United States. Li et al. (2017) used high-resolution WRF-Chem (0.6-, 1-, and 3-km) simulations to analyze the deep convective transport in three different convective regimes during the 2012 Deep Convective Clouds and Chemistry (DC3) field campaign (Barth et al., 2015) that featured air mass thunderstorms, a supercell severe storm, and a mesoscale convective system (MCS), respectively. They found that the convective transport patterns were different in the three convective regimes. For example, the rear inflow jets within the MCS weakened the convective transport of PBL trace gases.

Subgrid-scale convective transport of trace gases is an important component of cloud-parameterized simulations. Wang et al. (1996) evaluated the subgrid-scale and grid-scale convective transport in a tropical MCS during the Transport and Atmospheric Chemistry Near the Equator-Atlantic experiment at 90- and 30-km model resolution (two nested domains), and a midlatitude squall line during the Preliminary Regional Experiment for Storm-scale Operational and Research Meteorology at 75- and 25-km model resolution (two nested domains), and found that substantial subgrid transport occurred in the updraft (~41% of total upward transport in the MCS case and ~64% in the squall line case). Ott et al. (2009) compared vertical profiles of trace gases from simulations of storms during three field campaigns with a cloud-resolving model and a single-column model (SCM) implementation of version 5 of the Goddard Earth Observing System (GEOS-5) that utilized the relaxed Arakawa-Schubert cumulus parameterization. They found that the SCM simulations underpredicted convective mass flux and trace gas mixing ratios in the upper troposphere relative to the cloud-resolving model simulations. Also, they investigated the sensitivity of convective transport in the SCM to the values of parameters contained in the moist physics schemes. By tuning the most significant parameters influencing convective transport, the SCM simulation of trace gas mixing ratio was improved. Freitas et al. (2000) presented a parameterization of subgrid-scale convective transport of trace gases associated with deep moist convective systems for low-resolution atmospheric models. Grell and Freitas (2014) described a subgrid tracer transport and wet scavenging calculation method, which could be used in high-resolution nonhydrostatic mesoscale models.

The purpose of this study is to evaluate the parameterized convective transport of trace gases in WRF-Chem. The WRF model is a three-dimensional (3-D) compressible nonhydrostatic atmospheric modeling system designed for both meteorological research and numerical weather prediction. WRF-Chem (Grell et al., 2005) is WRF coupled with atmospheric chemistry and simulates the emission, transport, mixing, and chemical transformation of trace gases and aerosols simultaneously with the meteorology. The parameterized convective transport of trace gases in WRF-Chem has not previously been fully evaluated. Previous studies mostly focused on convective transport in older generation regional models (e.g., Wang et al., 1996). In this study, WRF-Chem is employed at cloud parameterized resolution to simulate two different convective regimes that occurred during the DC3 field campaign: a severe supercell thunderstorm and an MCS case. The purpose of this study is to evaluate the model-simulated subgrid convective transport and redistribution of trace gases in these two convective regimes through comparisons with aircraft observations and finer-resolution cloud-resolved simulations.

2. Observations

The 2012 DC3 field campaign was conducted from 15 May 15 to 30 June and sampled storms in three locations: (1) northeastern Colorado, (2) central Oklahoma to west Texas, and (3) northern Alabama. Three extensively instrumented aircraft platforms were utilized to gather in situ observations in the inflow and outflow regions of the convective storms: (1) the National Science Foundation (NSF)/National Center for

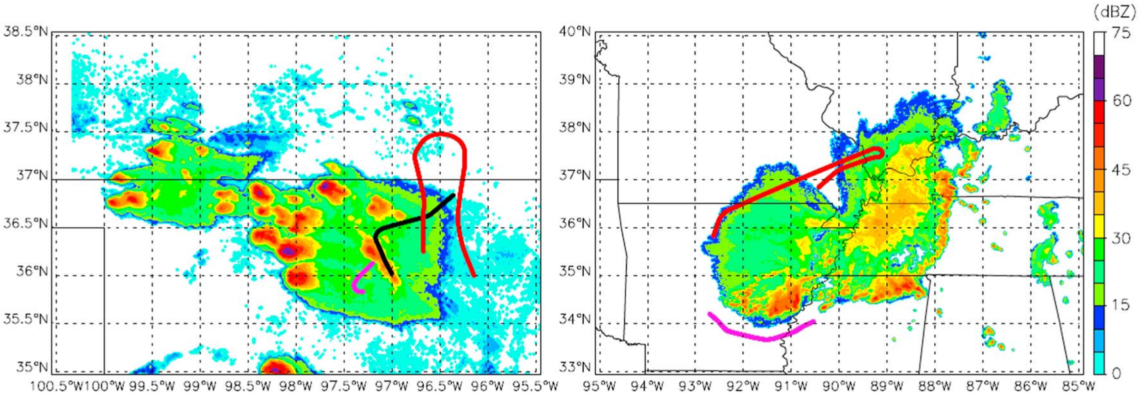

Figure 1. Column-maximum NEXRAD radar reflectivity contours (dBZ) at (a) 0000 UTC on 30 May 2012 and (b) 2200 UTC 11 June 2012. DC-8 inflow (magenta), DC-8 outflow (black), and GV outflow (red) sampling flight segments are shown by lines (*x* axis: longitude; *y* axis: latitude).

Atmospheric Research (NCAR) Gulfstream-V (GV) aircraft, (2) the National Aeronautics and Space Administration (NASA) DC-8 aircraft, and (3) the Deutsches Zentrum fur Luft- und Raumfahrt (DLR) Falcon aircraft. In order to be consistent with previous studies (Bela et al., 2016, 2018; Li et al., 2017), only the GV and DC-8 aircraft data are used in this study. Both aircraft measured a variety of gas phase species, aerosols, radiation, cloud particle characteristics, and meteorological properties. The radar data used in this study are from the NEXt generation weather RADar (NEXRAD)-Weather Surveillance Radar-1988 Doppler (WSR-88D), with a horizontal resolution of 0.02° latitude and longitude, a vertical resolution of 1 km, and a temporal resolution of 5 min (Homeyer et al., 2014). The 4-km National Centers for Environmental Prediction (NCEP) Stage IV data are used as precipitation observations in this paper.

3. Case Studies

In this research, we focus on the deep convective transport within convective systems sampled from two different convective regimes during the DC3 campaign: a supercellular storm system that initiated in Oklahoma on 29 May (Bela et al., 2016; DiGangi et al., 2016; Phoenix et al., 2017; Yang et al., 2015) and a linear MCS that took place in the central United States (over Missouri, Arkansas, and Illinois) on 11 June (Li et al., 2017). A DC3 air mass convective system observed in northern Alabama was simulated by Li et al. (2017) at cloud-resolved resolution; however, we do not consider that case here, as none of the convective parameterizations we applied in the WRF model (see section 4.2) were able to reproduce the two isolated cells of this system. This case was too small to reproduce on the 36-km-resolution domain. It had two isolated cells with the diameters of each cell being less than 50 km. Also, this system was surrounded by two much larger and stronger convective systems. Some schemes did not produce any evidence of the storm, while others initially simulated the storm, but the storm soon merged with the other surrounding stronger storms.

3.1. The 29 May Oklahoma Supercell Storm System

On 29 May, a thunderstorm system developed on the Oklahoma/Kansas border, around 2110 UTC, to the south of a quasi-stationary front near the Oklahoma and Kansas border (DiGangi et al., 2016). Two isolated cells initiated over northern Oklahoma and developed several updraft cores (Figure 1a). The DC-8 and GV aircraft started sampling the storm at ~2000 UTC before convective initiation (CI). The DC-8 aircraft measured the storm inflow from 2310 to 2315 UTC at 1.5-km height. At ~2330 UTC, the DC-8 spiraled up to sample the outflow on the eastern edge of the storm at ~10.8-km height (Figure 1a). Meanwhile, the GV measured the storm outflow at ~11.7 km from 2359 to 0023 UTC (Fried et al., 2016). More details on storm evolution and structure are shown in DiGangi et al. (2016), Bela et al. (2016), and Li et al. (2017).

3.2. The 11 June Central United States Mesoscale Convection System

The MCS initiated around 1900 UTC on 10 June. Several strong to severe thunderstorms developed along a line ahead of a sharp cold front that swept across Minnesota, North Dakota, South Dakota, and Nebraska. At around 0530 UTC on 11 June, the main convective line broke into two parts. The northern storm system

Table 1
WRF-Chem Model Configuration and Physics and Chemistry Options

	29 May supercell	MCS
Meteorology IC/BC	*NAM starting from 18 UTC*	*GFS starting from 06 UTC*
Chemistry IC/BC	*MOZART scaled*	*MOZART scaled*
Grid resolution	*36 km, 12 km*	
Vertical levels	*90*	
Time step	*120 s, 60 s*	
Cumulus scheme	*GF with KF closure*	*GF with all closure*
Microphysics	*Morrison*	
PBL	*MYJ*	*YSU*
Land surface	*Noah*	
Short/longwave radiation	*RRTMG*	
Chemistry option	*Chem_opt = 13 (No chemical reaction, run with five tracers)*	
Subgrid trace gases transport	*Subgrid convective transport calculation within the GF cumulus scheme based on the GF mass flux*	

began to decay, while the southern part that extended from Wisconsin across Iowa to Kansas gained more strength and started to move southeastward. This MCS was located in the Illinois-Missouri-Arkansas region when sampling started at 1600 UTC and moved southeast to the Kentucky and Tennessee region by 2300 UTC. The DC-8 measured the storm inflow on the southern edge of the MCS at 2200 UTC, and the GV sampled the storm outflow at ~12 km from 2200 to 2237 UTC (Figure 1b). For more details, the reader is referred to Li et al. (2017).

4. Model

The WRF-Chem V3.9 containing the Advanced Research WRF dynamic core (Skamarock & Klemp, 2008) was utilized to simulate the aforementioned two cases. The detailed model configuration and physics and chemistry options for the two cases are listed in Table 1. Model outputs at 10-min intervals were used for the analysis.

4.1. Model Configuration and Initial and Boundary Conditions

For both cases, WRF-Chem model simulations were conducted on two domains at cloud-parameterized scales (36- and 12-km horizontal grids, one-way nested, two domains were run simultaneously, Figure 2). There were 90 vertical levels with a 50-hPa model top. The time steps for each domain were 120 and 60 s, respectively.

We tried various initial conditions (IC) and boundary conditions (BC) for both cases. The best simulation for the 29 May supercell case was initialized on 29 May at 1800UTC using meteorological IC and BC derived from the 6-hourly 12-km North American Mesoscale Analysis. These IC and BC are the same as used in the cloud-resolved simulation by Li et al. (2017). For the 11 June MCS case, the best simulation was initialized on 11 June at 0600 UTC using IC and BC derived from the 6-hourly Global Forecast System analysis (GFS). The model output from the Model for Ozone and Related chemical Tracers, version 4 (MOZART-4) was used to generate the chemical IC and BC for both cases. However, for the 29 May supercell case, the MOZART CO mixing ratios were larger than aircraft observations, especially in the PBL. So we use the following equation to tune the 1–15-km CO IC, where the unit of CO is parts per billion volume (ppbv), and the unit of height is kilometers (km).

$$\mathrm{CO}_{\mathrm{MOZART\ Scaled}} = \frac{85+\mathrm{Height}}{100}\times \mathrm{CO}_{\mathrm{MOZART}} \tag{1}$$

For the 11 June MCS case, the MOZART CO mixing ratios were lower than aircraft observations. Therefore, the following equation was used to tune the 1–9-km CO IC.

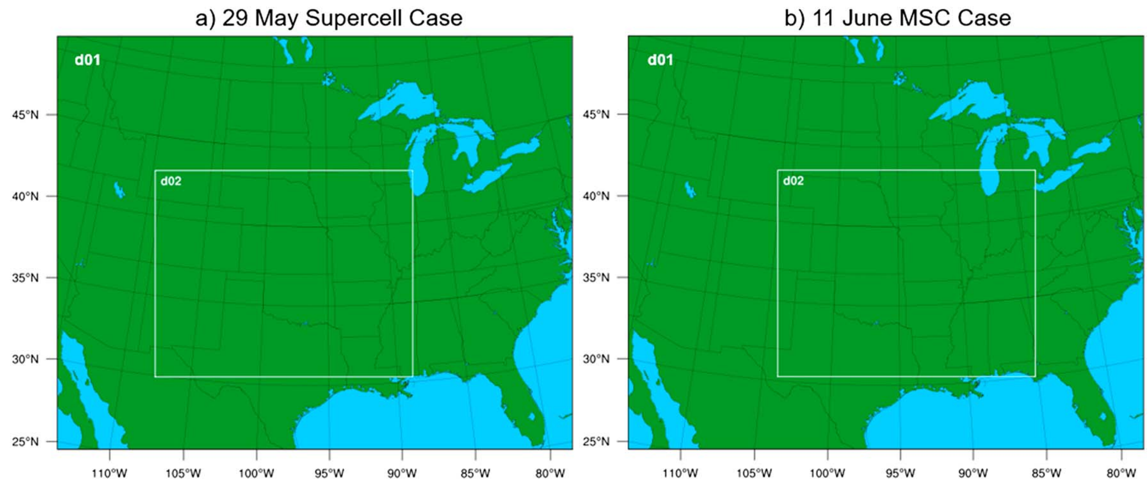

Figure 2. Nested domains for WRF-Chem simulations: (a) 29 May 2012 supercell case and (b) 11 June 2012 MCS case (*x* axis: longitude; *y* axis: latitude). Domain 1 (d01) has 36-km horizontal resolution, and domain 2 (d02) has 12-km resolution.

Table 2
Mean WRF-Chem Simulated Low-Level Inflow CO Mixing Ratios (ppbv) With One Standard Deviation Compared With Aircraft Measurements for 29 May Supercell Case and 11 June MCS Case

	29 May supercell	11 June MCS
Aircraft measurements	*132.3 ± 3.1*	*117.5 ± 4.3*
WRF-Chem 1 km	*136.3 ± 0.3*	*112 ± 7.8*
WRF-Chem 12 km	*131.3 ± 0.7*	*119.4 ± 3.9*
WRF-Chem 36 km	*131.7 ± 0.8*	*115.3 ± 3.8*

$$\mathrm{CO_{MOZART\ Scaled}} = \frac{109 - \mathrm{Height}}{100} \times \mathrm{CO_{MOZART}} \qquad (2)$$

For both cases, we did not modify the BC, as analysis of the simulations confirmed that no significant perturbations in CO concentration were advected into the analysis domains during the simulations. Table 2 shows the simulated CO inflow compared with aircraft-measured CO inflow. The aircraft-measured inflow was based on Fried et al. (2016). The simulated inflow was calculated along the inflow aircraft track. After tuning the CO IC, the observed inflow CO mixing ratio was reproduced well in all the simulations. The WRF-Chem simulated low-level inflow CO mixing ratios were evaluated against aircraft measurements. For both cases, the simulations of CO mixing ratios in low-level inflow were within 5% of the aircraft measurements (Table 2).

4.2. Cumulus Parameterization

The cloud-parameterizing WRF results were highly dependent on the choice of cumulus schemes, especially for the 29 May supercell case. In order to find the best performing cumulus scheme for these storms, we tried five commonly used cumulus parameterization options in WRF: (1) Kain-Fritsch (KF) scheme (Kain, 2004), which uses a mass flux approach with downdrafts and CAPE removal time scale; (2) Betts-Miller-Janjic (BMJ) scheme (Janjić, 1994, 2000), a scheme which relaxes the column moisture profile toward a well-mixed profile; (3) Grell-Freitas (GF) scheme (Grell & Freitas, 2014), which is a scale-aware scheme based on the Grell-Devenyi (GD) scheme (details in section 4.5); (4) Grell-3D (G3) scheme (Grell, 1993; Grell & Devenyi, 2002), which is an improved version of the GD scheme (a multiclosure, multiparameter, ensemble method) that may also be used on high resolution; and (5) Tiedtke scheme (Tiedtke, 1989; Zhang et al., 2011), which is a mass flux type scheme with CAPE-removal time scale, shallow component, and momentum transport.

4.3. Other Physics Options

The PBL option was Mellor-Yamada-Janjic scheme (Janjić, 1994) for the 29 May supercell case and Yonsei University (YSU) scheme (Hong et al., 2006) for the 11 June MCS case. The choice of PBL scheme was based on the one that yielded the best precipitation simulation. For both cases, the other main physics choices were the two-moment Morrison microphysics (Morrison et al., 2009) for microphysical processes, the Rapid Radiative Transfer Model for General Circulation Models (RRTMG) scheme (Iacono et al., 2008) for longwave and shortwave radiation, and the Noah scheme (Koren et al., 1999) for land surface processes.

4.4. Preliminary Precipitation Results

Figure 3 shows the precipitation during the 3-hr period after CI was observed (observation: 2100–0000 UTC; KF: 1850–2150 UTC; BMJ: 2220–0120 UTC; GF: 2220–0120 UTC; G3D: 2040–2340 UTC; and Tiedtke: 2300–0200 UTC) for the 29 May supercell case. NCEP Stage IV precipitation observations averaged to the 36-km grid are compared with results from model simulations using the five cumulus parameterizations discussed in section 4.2. The observations show a two-cell structure with precipitation maxima in excess of 10 mm. The KF scheme did not reproduce the two-cell structure of the observed storm. The BMJ and G3 schemes underestimated the precipitation maxima. Although the Tiedtke scheme captured the two-cell structure of the storm and the maximum precipitation was close to observations, the simulated precipitation region was too small. Compared with the other results, the model simulation of the 3-hr precipitation location and strength were the best when using the GF scheme.

Although the 3-hr total precipitation of the GF simulation well matched the observations, the 1-hr maximum precipitation at the aircraft measuring time (3 hr after CI) was ~36.5% lower than the observations. In order to improve the maximum 1-hr precipitation simulation for the 29 May supercell case, we tried tuning the closure options inside the GF scheme following Qiao and Liang (2015, 2016, 2017) who examined the effects of major cumulus parameterization closures on simulation of summer precipitation. They found that closure algorithms largely affect precipitation's geographic distribution, frequency and intensity, and diurnal cycle, with strong regional dependence. There are four major groups of closure assumptions used in the original GF scheme: the Arakawa and Schubert (AS) closure, the vertical velocity (W) closure, the Kain and Fritsch (KF) closure, and the moisture convergence (MC) closure. The AS closure (Arakawa & Schubert, 1974)

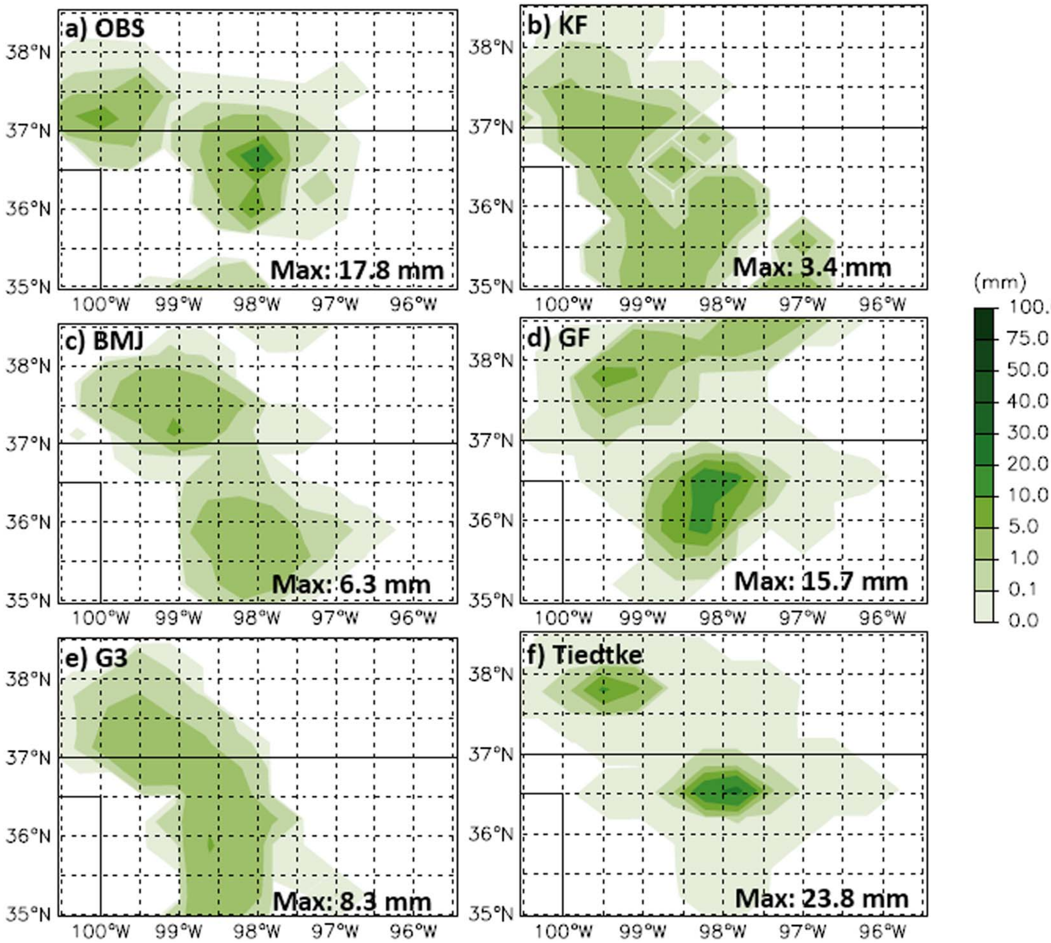

Figure 3. Three-hour precipitation (mm) for the 29 May supercell case, at 36-km resolution from the start of the convection for (a) observations (2100–0000 UTC), (b) WRF-Chem with KF cumulus scheme (1850–2150 UTC), (c) BMJ cumulus scheme (2220–0120 UTC), (d) GF cumulus scheme (2220–0120 UTC), (e) G3 cumulus scheme (2040–2340 UTC), and (f) Tiedtke cumulus scheme (2300–0200 UTC; (*x* axis: longitude; *y* axis: latitude), with 3-hr maximum precipitation (mm) labeled in the right bottom corner (the plotting routine includes interpolation, which leads to the structures smaller than the model resolution).

determines the cloud base mass flux (CBMF) by adjusting the cloud work function toward a climatological value to maintain instantaneous equilibrium between large-scale forcing and subgrid convection. The W closure (Brown, 1979; Frank & Cohen, 1987) calculates the CBMF using the environmental vertical velocity at lower tropospheric levels. In the MC closure (Krishnamurti et al., 1983), the calculation of the CBMF is based on moisture convergence. In the KF closure (Kain & Fritsch, 1993), the calculation of the CBMF is based on the assumption that the CAPE is simply removed by the convection over a specific time period. The original GF scheme uses an average CBMF from the results of the above closures.

Table 3
The Observations and WRF-Chem Simulations of the Maximum Precipitation per Hour (mm/hr) for 29 May Supercell Case at 1 to 3 hr After CI

	1 hr after CI	2 hr after CI	3 hr after CI
OBS	*1.84*	*4.53*	*16.87*
WRF-Chem with all four closures in GF	*3.83*	*6.17*	*10.71*
WRF-Chem with AS closure in GF	*3.28*	*5.42*	*14.68*
WRF-Chem with W closure in GF	*3.57*	*6.26*	*12.44*
WRF-Chem with MC closure in GF	*3.62*	*6.28*	*10.64*
WRF-Chem with KF closure in GF	*2.00*	*4.38*	*16.03*

We reran the WRF simulation four times with only one closure turned on at each time. Then we compared the observed and simulated first 3-hr maximum hourly precipitation, as the majority of convective transport is in the high-precipitation region (Li et al., 2017). The results are listed in Table 3. The maximum hourly precipitation simulation with the KF closure closely matched the observed maximum hourly precipitation (the difference is within 5% of the observations). Therefore, we regarded the KF closure simulation as the best result, and our following analysis of the 29 May supercell case was based on this simulation. For the 11 June MCS case, the simulation with the original GF scheme performed well. Therefore, we did not test the performance of using different closures for this case, and the results in section 5 use the normal GF scheme.

4.5. Chemistry Option and Subgrid Convective Transport Option

The chemistry option for both cases was option 13 (no chemical reaction, run with six tracers: SO_2, CO, NO, higher aldehydes, CH_2O, and organic acids; we only use CO in this paper) without emission. Within WRF-Chem a routine separate from the transport of water vapor in WRF is used to calculate the fluxes for the chemical species and tracers. The default subgrid convective transport scheme inside the WRF-Chem is based on the GD convection scheme, which is not consistent with our WRF-Chem simulation with GF cumulus scheme. Therefore, we discuss the differences between the GD and GF schemes in the paragraphs below, as well as our solution to the transport inconsistency.

The GD mass flux cumulus scheme (Grell & Devenyi, 2002) is based on a convective parameterization developed by Grell (1993) and Grell et al. (1994) but expanded to include options for a series of different assumptions that are commonly used in modern convective parameterizations. The GD scheme uses an ensemble of 144 members with different static and dynamic controls (Skamarock et al., 2008). The static controls are based on different updraft and downdraft entrainment and detrainment parameters and precipitation efficiencies. These differences in static control are combined with differences in dynamic control, which is the method of determining cloud mass flux. The dynamic control closures are based on convective available potential energy (CAPE or cloud work function), low-level vertical velocity, or moisture convergence. Another control is the trigger, where the maximum cap strength that permits convection can be varied. The results are averaged over the ensemble to give the feedback to the model. For more details, the reader is referred to Grell and Devenyi (2002), Grell (1993), Grell et al. (1994), and Skamarock et al. (2008).

The GF scheme is based on the older GD scheme with several modifications. First, the GF scheme reduces the size of the ensemble. Only the dynamic controls (closures) and the maximum cap strength trigger control are kept in the GF scheme. Second, in the GD scheme, the nonresolved flux for one ensemble member is based on the results of that ensemble member, while in the GF scheme, the nonresolved flux for one ensemble member is based on the average results of all the ensemble members. Third, the GF scheme parameterizes the convection on *almost* cloud-resolving scales by two approaches. The first approach includes the unified parameterization of deep convection proposed by Arakawa et al. (2011) to calculate the convective vertical eddy transport at varying horizontal scales. The second approach spreads the subsidence over the neighboring grid cells. Furthermore, the GF scheme includes a new closure based on Bechtold et al. (2014) to improve the simulation of the diurnal cycle. In addition, although not employed in the current analysis, the GF scheme is capable of representing aerosol cloud interaction (Grell & Freitas, 2014).

Grell and Freitas (2014) also provide a method to calculate the subgrid convective transport of trace gases. However, this method was not used in WRF-Chem, as this method requires the subgrid convective transport of trace gases calculation to be calculated in the physics module, as opposed to the chemistry module where it is calculated by default in WRF-Chem. Therefore, in the unmodified WRF-Chem model the calculation of convective transport of trace gases in the chemistry module, which is done using the GD cumulus parameterization, is separate and independent from the calculation of the convective transport of mass and moisture in the physics module. As shown in section 4.4, the simulated storm location, size, and strength when using different cumulus parameterizations are very different from each other. Thus, if the cumulus parameterization used in the calculation of the convective transport of trace gases is inconsistent with the cumulus parameterization used in the meteorology module, it will lead to convective transport of trace gases into regions where the mass and moisture fields do not feel the effect of convection and/or to a mismatch between the strength of convection affecting the trace gases and the mass/moisture fields. In order to be consistent with the cumulus parameterization in the meteorological module, we rewrote the module of subgrid convective transport of trace gases and moved the module from the chemistry part of the WRF-Chem model to the physics part of the model (Li, 2018). The mass flux-related variables (i.e., entrainment and detrainment rate, cloud top height, CBMF, downdraft mass flux, updraft mass flux, the originating level of updraft and downdraft, level of free convection, evaporation, and precipitation) from GF scheme were used to calculate the subgrid convective transport of trace gases in the new routine using the following equation (Grell & Freitas, 2014):

$$\left(\frac{\partial C}{\partial t}\right)_{\text{subgrid}} = -\frac{1}{\rho}\frac{\partial}{\partial z}\left[m_u(C_u - C_e) - m_d(C_d - C_e) + m_u C_{\text{aq}}\right] - \overline{C_{\text{si}}} + \overline{C_{\text{so}}} \tag{3}$$

where C represents the mass mixing ratio of CO, ρ represents air density, and m represents mass flux. The subscripts e, u, and d represent the environment, updraft, and downdraft, respectively. C_{aq} represents the chemical constituent in the aqueous phase, C_{so} is calculated using an aqueous phase chemistry routine (source), and C_{si} depends on the conversion rate of cloud water to rain water and the solubility of the tracer (sink). In this paper, we focus on the convective transport of an insoluble trace gas (CO). Thus, equation (4) can be simplified to

$$\left(\frac{\partial C}{\partial t}\right)_{\text{subgrid}} = -\frac{1}{\rho}\frac{\partial}{\partial z}\left[m_u(C_u - C_e) - m_d(C_d - C_e)\right] \tag{4}$$

5. Results

5.1. Evaluation of Precipitation Results

For the 29 May supercell case, the model with GF subgrid convection with KF closure (GF-KF run) produced a storm that began 80 (for the simulations at 36-km resolution) and 30 min (for the simulations at 12-km resolution) later than the observations. Because the 12-km convection started earlier, the 36-km parameterized convection did not affect the initiation of convection at 12 km. The 3-hr precipitation observations at 0000 UTC and model simulation at 0120 UTC (for the simulations at 36-km resolution) and at 0030 UTC (for the simulations at 12-km resolution) on 30 May are compared in Figure 4. Both the 36- and 12-km WRF-Chem simulations capture the storm location, precipitation strength, and the two-cell structure of the storm. Comparison of the middle four panels (Figures 4c–4f) indicates that the precipitation for the 36-km-resolution simulation is mainly subgrid scale (subgrid-scale mean precipitation is 2.8 times greater than grid-scale mean precipitation), while the precipitation for the 12-km-resolution simulation is mainly grid scale (grid-scale mean precipitation is 2.5 times greater than subgrid-scale mean precipitation). Therefore, in the 36-km run, subgrid-scale convection dominates, while in the 12-km run, grid-scale convection dominates.

The precipitation results with the GF scheme and the standard closure procedure for the 11 June MCS case are shown in Figure 5. Both 36- and 12-km WRF-Chem simulations capture the storm location and the strong precipitation region. In the 12-km simulation, the precipitation amount (Figure 5h) is larger than the observations, which is caused by the overestimate of the grid-scale precipitation in the microphysics processes (Figure 5f). Also, in the 36-km run, subgrid-scale convection dominates (subgrid-scale mean precipitation is 4 times greater than grid-scale mean precipitation), and in the 12-km run, grid- and subgrid-scale convection make similar contributions (grid-scale mean precipitation is 1.1 times greater than subgrid-scale mean precipitation). The simulated precipitation rate in the storm core region is within 10% of the observations. In the southwest side of the storm, the area of the weak precipitation region in both the 36- and 12-km simulations is larger than in the observations. However, this will not have much influence on our convective transport analysis, as the majority of convective transport occurred in the storm core region after the storm became mature. Li et al. (2017) found that after the storm became mature, the convective transport in the storm core region, where composite reflectivity was higher than 40 dBZ, was a factor of 2–5 larger than the convective transport outside the core region.

5.2. Evaluation of the Convective Transport

We compared the cloud-parameterized convective transport with the cloud-resolved simulation, by comparing the observed and simulated high-level outflow CO mixing ratios in these regions. The cloud-resolved simulations we use here for the 29 May supercell and the 11 June MCS are described in Bela et al. (2016) and Li et al. (2017), respectively, and the model set up and evaluation. The resolution for the cloud-resolved simulation was 1 km for the 29 May supercell case and 3 km for the June 11 MCS case. For both cases, the storm location, size, and structure (intensity, anvil height, and extent) were well represented by the cloud-resolved simulation results. The simulated chemistry fields were reasonably consistent with observations for the two cases. The model-simulated CO mixing ratio was within 5% of the aircraft measurements in the low-level inflow region and 1% of the aircraft measurements in the upper level outflow region.

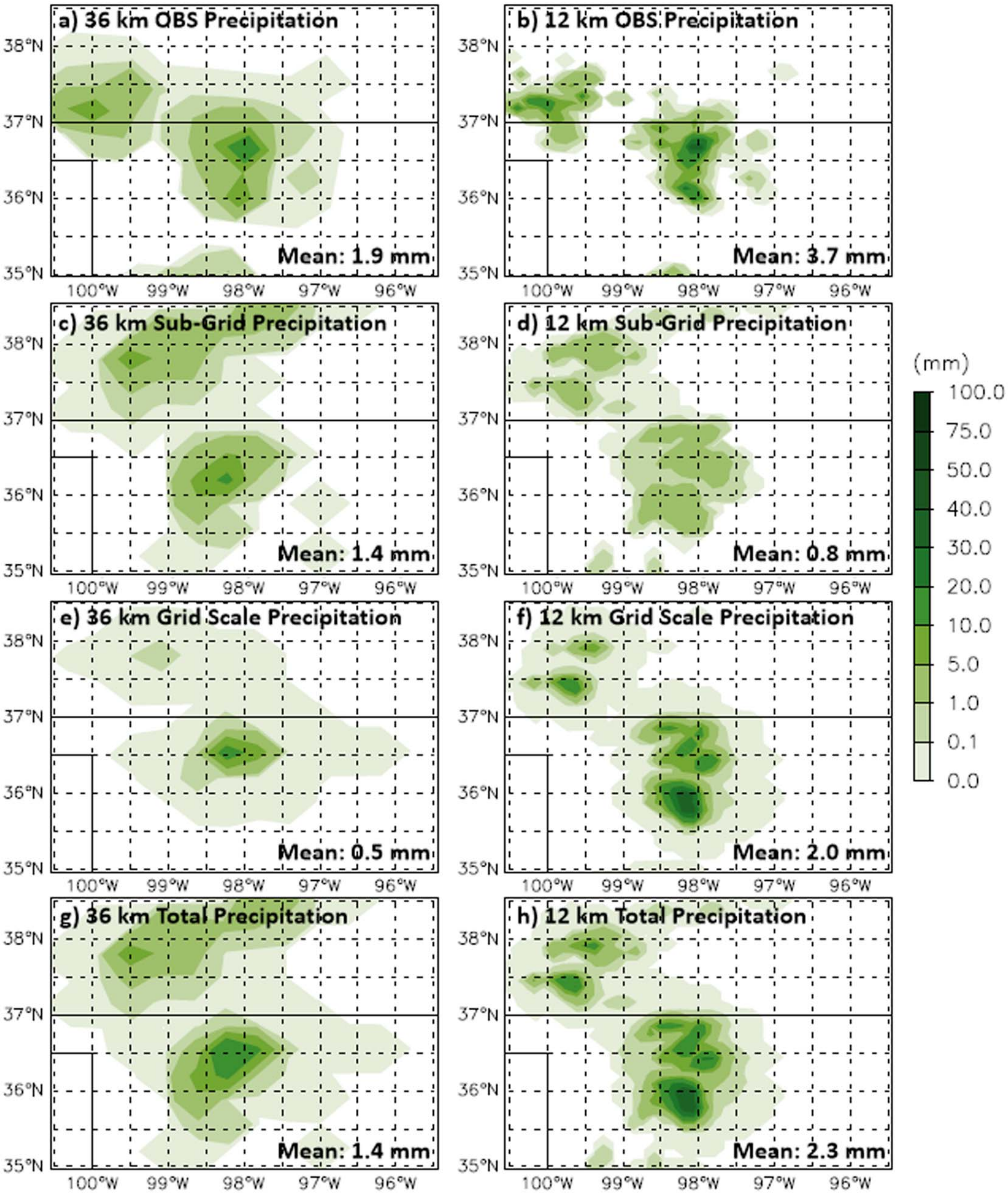
a) 36 km OBS Precipitation
Mean: 1.9 mm
b) 12 km OBS Precipitation
Mean: 3.7 mm
c) 36 km Sub-Grid Precipitation
Mean: 1.4 mm
d) 12 km Sub-Grid Precipitation
Mean: 0.8 mm
e) 36 km Grid Scale Precipitation
Mean: 0.5 mm
f) 12 km Grid Scale Precipitation
Mean: 2.0 mm
g) 36 km Total Precipitation
Mean: 1.4 mm
h) 12 km Total Precipitation
Mean: 2.3 mm
38°N
37°N
36°N
35°N
100°W
99°W
98°W
97°W
96°W
(mm)
100.0
75.0
50.0
40.0
30.0
20.0
10.0
5.0
1.0
0.1
0.0

Figure 4. Three-hour precipitation observations (mm) averaged to (a) 36-km grid and (b) 12-km grid at 0000 UTC on 30 May 2012; (c) WRF-Chem simulated 36-km subgrid scale, (e) grid scale(e), and (g) total precipitation at 0120 UTC on 30 May 2012; and (d) WRF-Chem simulated 12-km subgrid scale, (f) grid scale, and (h) total precipitation at 0030 UTC on 30 May 2012 (*x* axis: longitude; *y* axis: latitude).

In order to better evaluate the influence of the subgrid-scale convection on the outflow CO mixing ratio, we conducted three sensitivity test runs for the cloud-parameterized simulation: (1) using our new GF subgrid-scale convective transport scheme (hereafter GFCT scheme), (2) using the original WRF-Chem GD subgrid-scale convective transport scheme (hereafter GDCT scheme), and (3) no subgrid convective transport (hereafter NoCT). For the 29 May case, both the DC-8and GV measured storm outflow. The DC-8 measured storm outflow at ~10.8 km (average GPS height, Figure 6a); at the same time, the GV measured storm outflow at ~11.7 km (average GPS height, Figure 7a). For the 11 June case, the storm outflow region was only measured by the GV at an altitude of about 13 km (Figure 8a). Figures 6–8 compare the simulated high-level outflow CO field with the aircraft measurements at the mean aircraft flight altitude. In each of the figures the outflow CO aircraft measurements are plotted on the CO simulation field. Figures 9 and 10 compare the mean

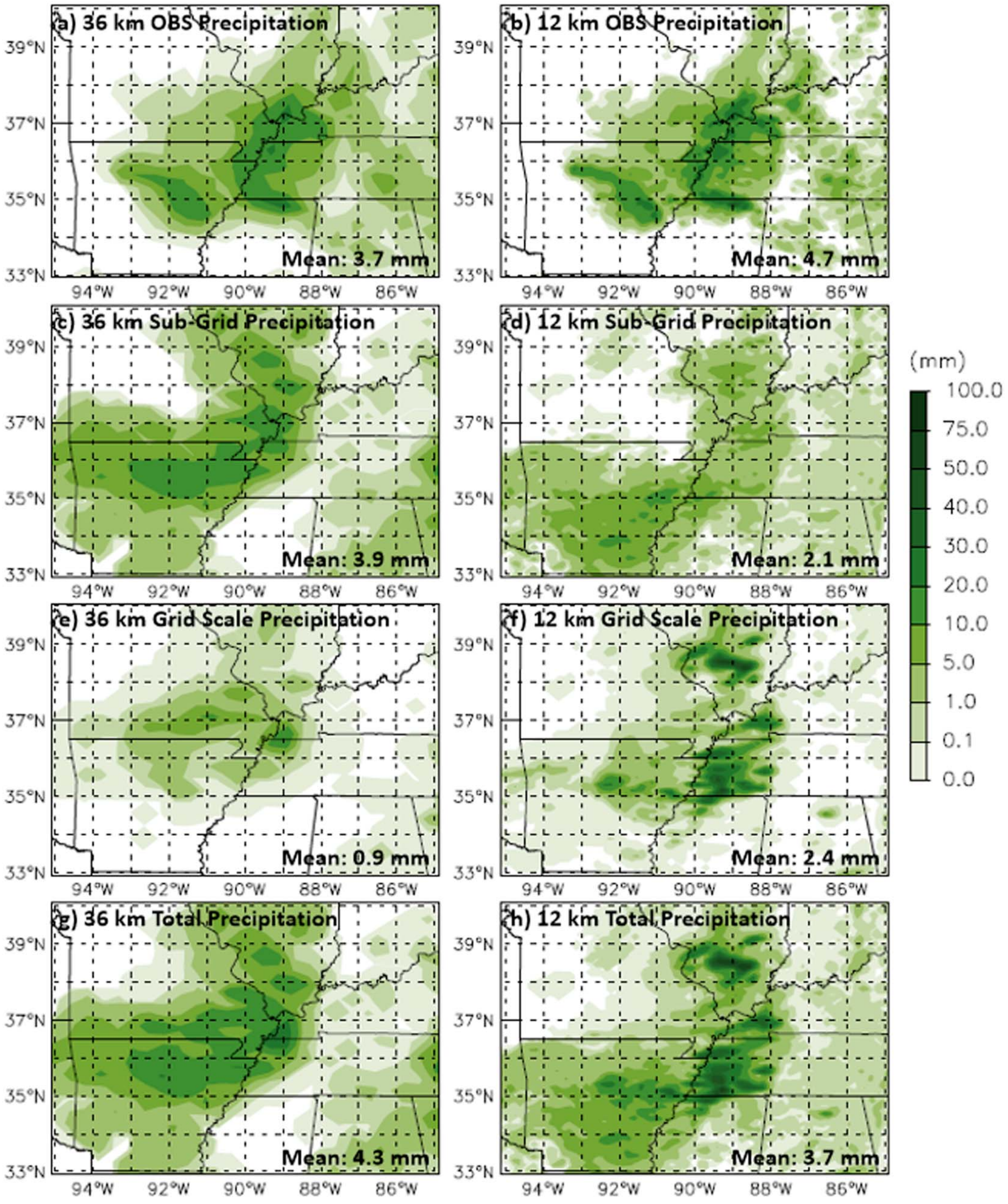
a) 36 km OBS Precipitation
Mean: 3.7 mm
b) 12 km OBS Precipitation
Mean: 4.7 mm
c) 36 km Sub-Grid Precipitation
Mean: 3.9 mm
d) 12 km Sub-Grid Precipitation
Mean: 2.1 mm
e) 36 km Grid Scale Precipitation
Mean: 0.9 mm
f) 12 km Grid Scale Precipitation
Mean: 2.4 mm
g) 36 km Total Precipitation
Mean: 4.3 mm
h) 12 km Total Precipitation
Mean: 3.7 mm
39°N
37°N
35°N
33°N
94°W
92°W
90°W
88°W
86°W
(mm)
100.0
75.0
50.0
40.0
30.0
20.0
10.0
5.0
1.0
0.1
0.0

Figure 5. Similar to Figure 4 but at 2200 UTC on 11 June 2012 for both observations and WRF-Chem simulation (*x* axis: longitude; *y* axis: latitude).

aircraft measured in-cloud CO vertical profiles with the simulated CO profiles averaged along the aircraft track and extended in height. The in-cloud points are defined as grid boxes where the total liquid and ice mixing ratio is greater than 0.01 g/kg or the altitude is lower than the cloud top height calculated in the cumulus parameterization.

For the 29 May supercell case, the cloud-resolved model-simulated CO mixing ratio was close to the observation (Figures 6b and 7b) in the storm outflow region. In the storm core region, which was outside the aircraft measuring region, the cloud-resolved simulated CO mixing ratio reached values larger than 140 ppbv at both DC8 and GV measuring heights, which was much larger than the simulated CO mixing ratio in the outflow region (~121 ppbv at DC8 measuring height and 109 ppbv at GV measuring height). For the cloud-parameterized run, the comparison of the three simulations indicated that the application of the GFCT scheme improved the model simulation of the upper level outflow CO, especially for the 36-km runs

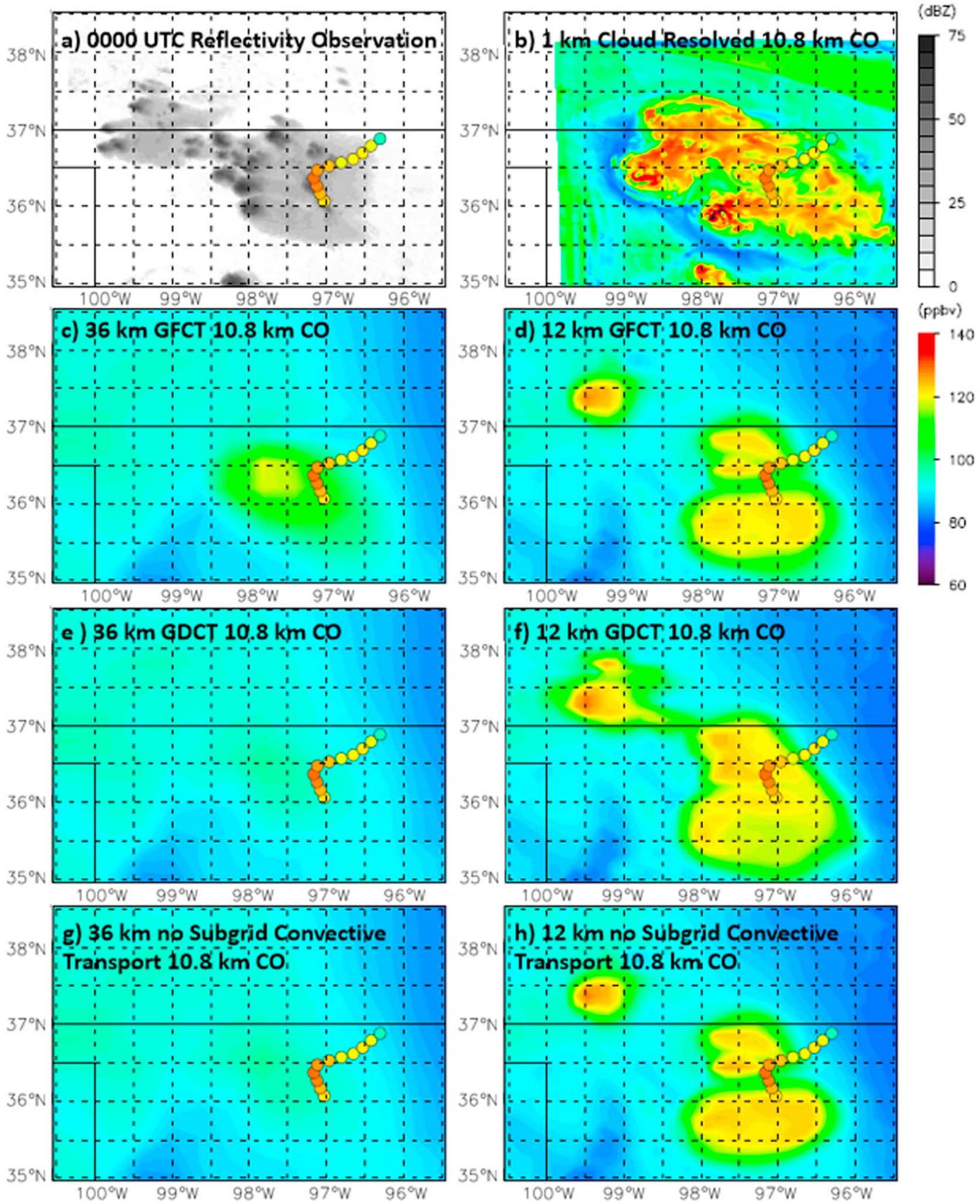
a) 0000 UTC Reflectivity Observation
b) 1 km Cloud Resolved 10.8 km CO
c) 36 km GFCT 10.8 km CO
d) 12 km GFCT 10.8 km CO
e) 36 km GDCT 10.8 km CO
f) 12 km GDCT 10.8 km CO
g) 36 km no Subgrid Convective Transport 10.8 km CO
h) 12 km no Subgrid Convective Transport 10.8 km CO
38°N
37°N
36°N
35°N
100°W
99°W
98°W
97°W
96°W
(dBZ)
75
50
25
0
(ppbv)
140
120
100
80
60

Figure 6. DC-8 measured outflow CO mixing ratio in ppbv at ~10.8-km altitude between 2348 and 2358 UTC on 29 May 2012 (colored dots). Background shading shows (a) 0000-UTC NEXRAD composite reflectivity (dBZ). (b) Background colors show 0040 UTC 1-km cloud-resolved simulation of 10.8-km CO mixing ratio, (c) 0120-UTC 36-km cloud-parameterized simulation of 10.8-km CO mixing ratio with GFCT, (e) GDCT, and (g) without subgrid convective transport; (d) 0030-UTC 12-km cloud-parameterized simulation of 10.8-km CO mixing ratio with GFCT, (f) GDCT, and (g) without subgrid convective transport (*x* axis: longitude; *y* axis: latitude).

(Figures 6c, 6e, 6g, 7c, 7e, and 7g). In the simulation results at 36-km resolution, both the GDCT run and the NoCT run failed to simulate the increase of CO associated with the outflow (Figures 6e, 6g, 7e, and 7g). The GFCT run successfully simulated a CO increase in the upper level CO outflow region (Figures 6c and 7c). Although the GFCT scheme improved the outflow CO simulation, the 36-km cloud-parameterized CO mixing ratios were still smaller than the aircraft observations and the cloud-resolved CO mixing ratios, especially in the storm core region. The cloud-parameterized CO outflow region was smaller in area than observed and simulated by the cloud-resolved model. We tried to tune the 36-km entrainment profile to

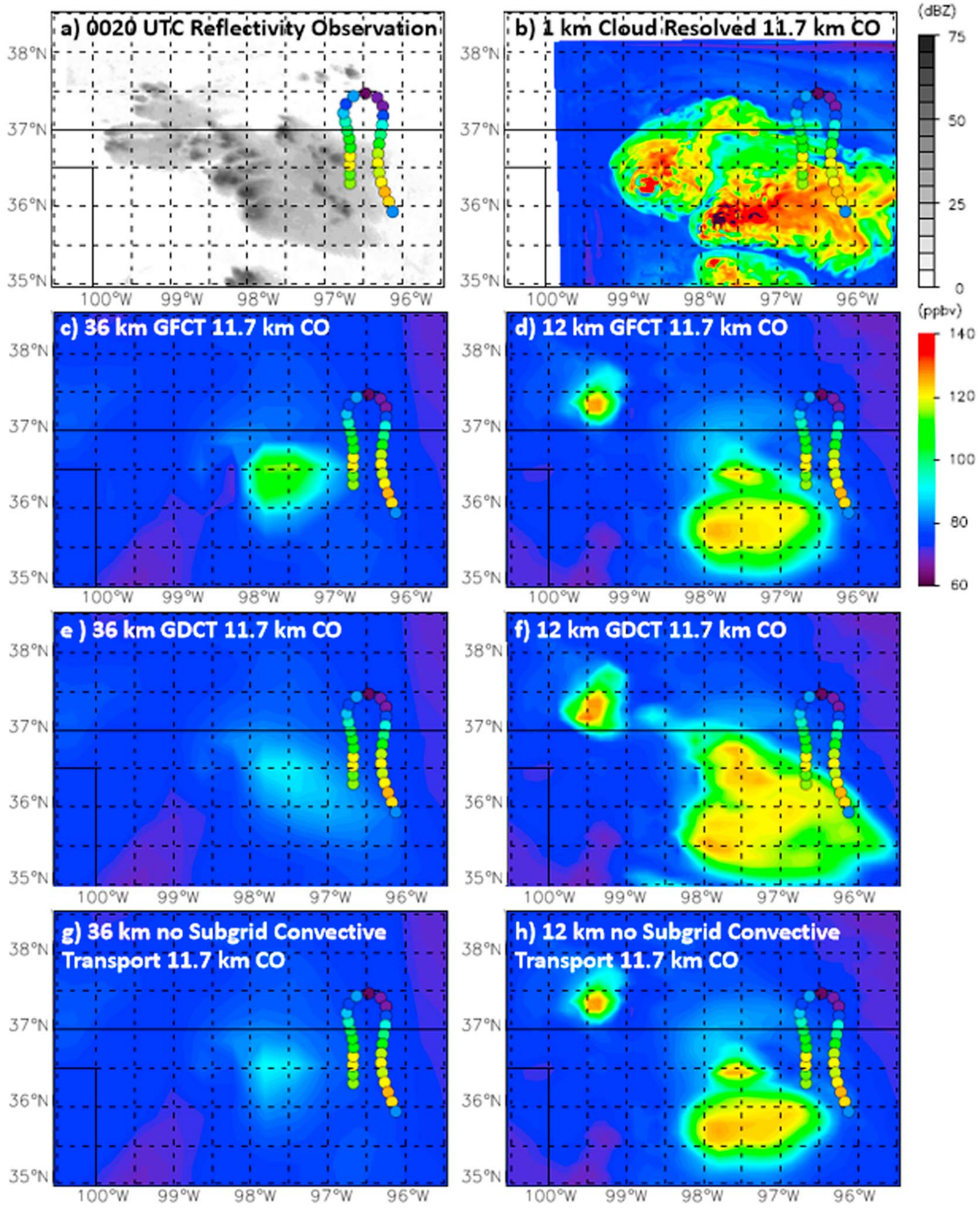
a) 0020 UTC Reflectivity Observation
b) 1 km Cloud Resolved 11.7 km CO
c) 36 km GFCT 11.7 km CO
d) 12 km GFCT 11.7 km CO
e) 36 km GDCT 11.7 km CO
f) 12 km GDCT 11.7 km CO
g) 36 km no Subgrid Convective Transport 11.7 km CO
h) 12 km no Subgrid Convective Transport 11.7 km CO
(dBZ)
75
50
25
0
(ppbv)
140
120
100
80
60
38°N
37°N
36°N
35°N
100°W
99°W
98°W
97°W
96°W

Figure 7. Similar to Figure 6 but for GV measured outflow at 11.7 km between 0000 and 0023 UTC on 30 May 2012 (colored dots); the NEXRAD data were at 0020 UTC, the cloud-resolved simulation result sampled at 0100 UTC, the 36-km simulations sampled at 0140 UTC, and the 12-km simulations sampled at 0050 UTC (*x* axis: longitude; *y* axis: latitude).

match observations (Fried et al., 2016) and the cloud-resolved simulation (Bela et al., 2018) but had little success. In the 12-km runs, the CO mixing ratio results from the three cloud-parameterized runs looked similar (Figures 6d, 6f, 6h, 7d, 6f, and 6h). This is because the 12-km convection simulation was dominated by the grid-scale convection as discussed in section 5.1. For the 29 May supercell case, the 12-km simulated CO outflow region was still smaller than aircraft observations but was much larger than that based on the 36-km outflow region.

When comparing the observation and simulated vertical profiles of in-cloud CO mixing ratio (Figure 9) for the 29 May supercell case, we shifted the cloud-arameterized model profile 0.75° west to sample the maximum of

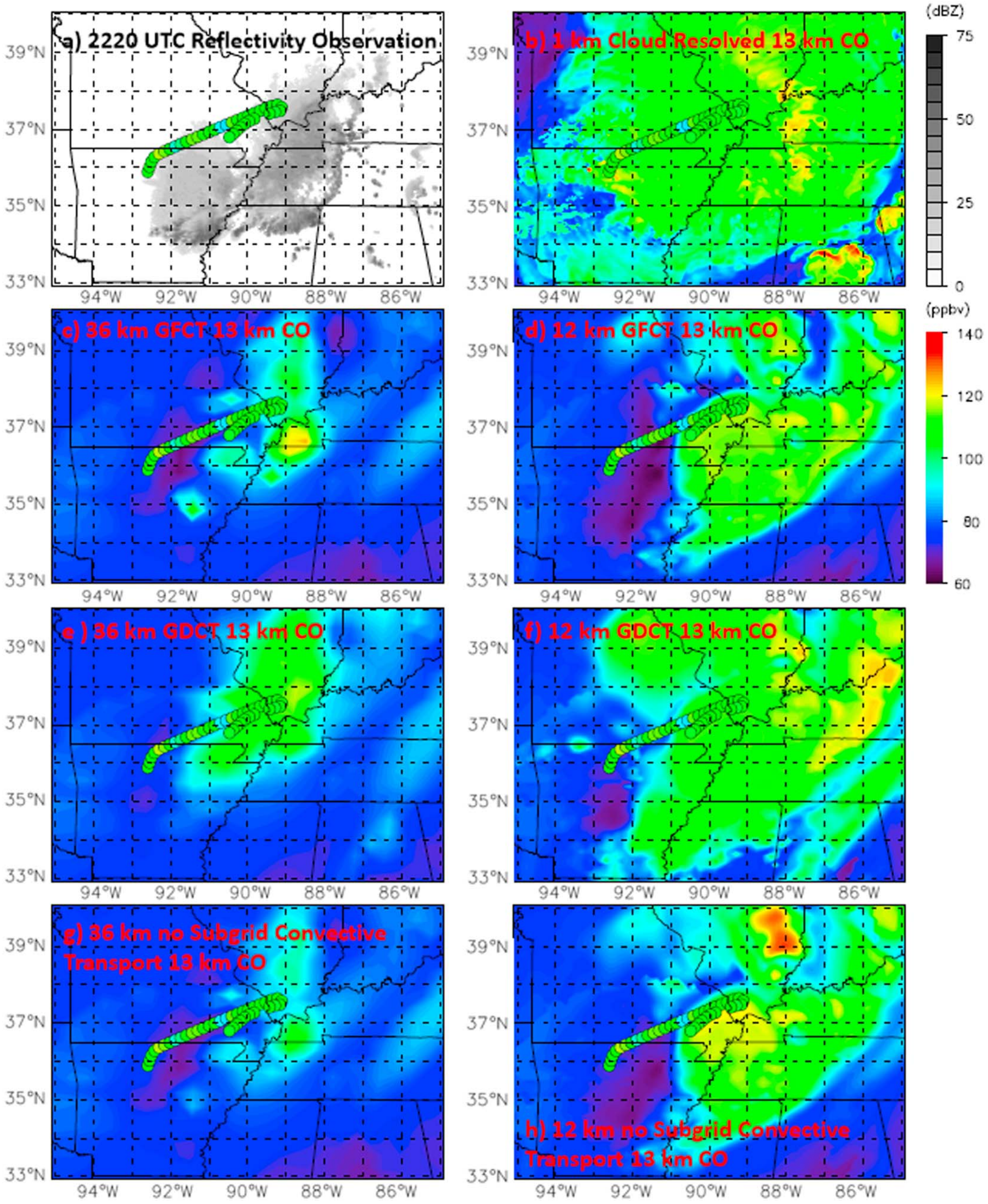
a) 2220 UTC Reflectivity Observation
b) 1 km Cloud Resolved 13 km CO
c) 36 km GFCT 13 km CO
d) 12 km GFCT 13 km CO
e) 36 km GDCT 13 km CO
f) 12 km GDCT 13 km CO
g) 36 km no Subgrid Convective Transport 13 km CO
h) 12 km no Subgrid Convective Transport 13 km CO
39°N
37°N
35°N
33°N
94°W
92°W
90°W
88°W
86°W
(dBZ)
75
50
25
0
(ppbv)
140
120
100
80
60

Figure 8. Similar to Figure 6 but for GV measured at 13 km between 2200 and 2237 UTC on 11 June 2012 (colored dots); the NEXRAD reflectivity and cloud-resolved and parameterized simulation results sampled at 2220 UTC (*x* axis: longitude; *y* axis: latitude).

the model outflow, as the anvil associated with the simulated storm with cloud parameterization was smaller than the observed and cloud-resolved anvils. The mean DC8-measured in-cloud CO mixing ratio between 10.75 and 11.25 km was ~119 ppbv, and the mean GV-measured in-cloud CO mixing ratio between 11.75 and 12.25 km was ~111 ppbv. In all three 36-km runs (Figure 9a), the midlevel and high-level in-cloud CO mixing ratio increased compared to the IC (between 7 and 12 km); however, only the GFCT run reproduced the in-cloud CO mixing ratio peak in the UT (between 10.5 and 12 km), which suggested that the convective transport in the GFCT scheme transports the PBL in-cloud CO to the UT more effectively. At the DC8 measuring level, the GFCT-simulated mean in-cloud CO mixing ratio was 115 ppbv, which was 18 ppbv (18.5%) greater than the GDCT and NoCT results (97 ppbv) but still 4 ppbv less than the DC8-measured CO mixing ratio. At the GV measuring level, the GFCT-simulated mean in-cloud CO mixing ratio

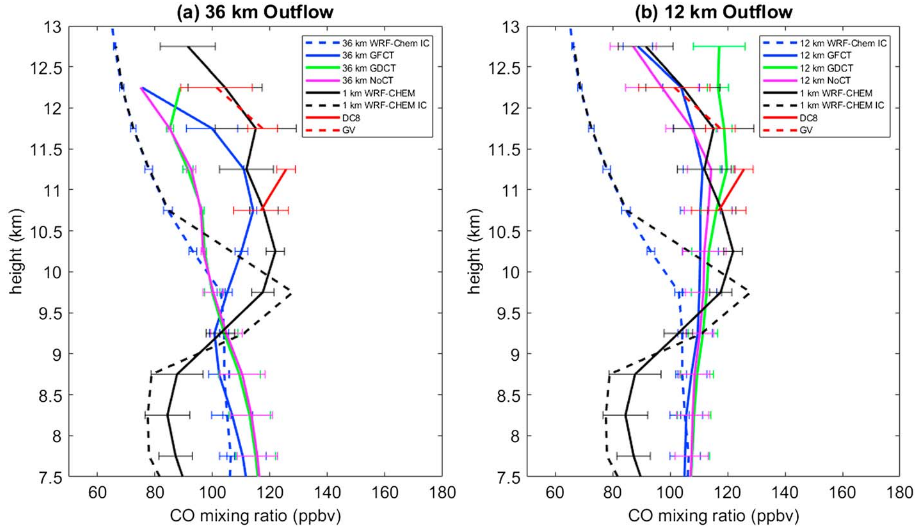

Figure 9. Mean outflow CO profiles from the 29 May supercell storm as observed by the DC-8 (red solid line) and GV (red dash line) aircraft, mean profiles as simulated in the (a) 36- and (b) 12-km-resolution WRF-Chem run with GFCT (blue), GDCT (green), NoCT (magenta), and mean profiles as simulated in the 1-km cloud-resolved WRF-Chem run (black), compared with the IC for cloud-parameterized run (blue dash) and cloud-resolved run (black dash). The error bars indicate one standard deviation. Model profiles shifted in horizontal with respect to the aircraft profiles by 0.75° to the west to ensure sampling of model outflow. Bela et al. (2016) used DC8 measurements to create a horizontally homogeneous IC for CO in a limited domain cloud-resolved model. Since our cloud-parameterized domain was much larger than Bela et al. (2016), we used MOZART to create the IC for our 36- and 12-km runs.

was 94 ppbv, which was 14 ppbv (17.6%) greater than NoCT result (80 ppbv), and 7 ppbv (8%) greater than GDCT results (87 ppbv), but still 17 ppbv less than the GV-measured CO mixing ratio. Unlike the result of the simulations at 36-km resolution, the cloud-parameterized in-cloud CO outflow mixing ratio simulation at 12-km resolution matched the observations well (Figure 9b). The differences among the three runs (GFCT, GDCT,

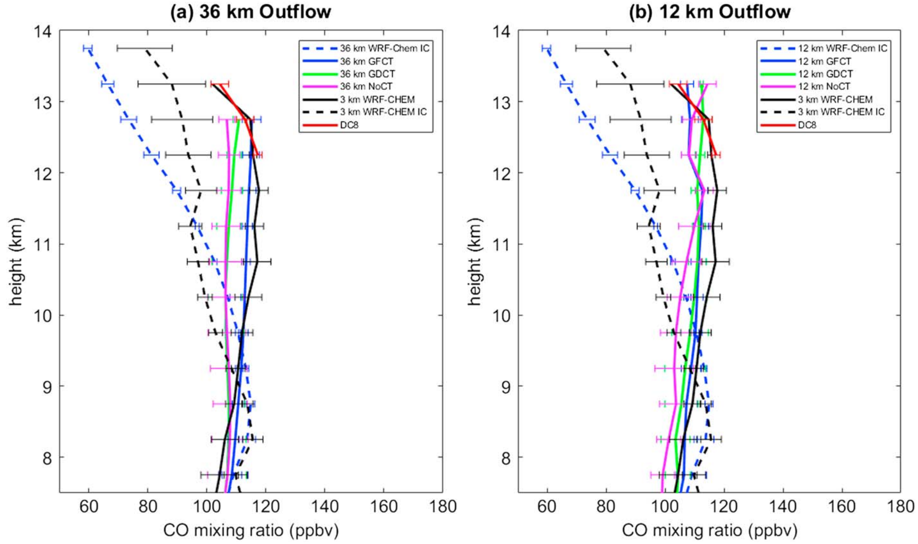

Figure 10. Mean outflow CO profiles from the 11 June MCS case as observed by the DC-8 (red solid line) aircraft, mean profiles as simulated in the (a) 36- and (b) 12-km-resolution WRF-Chem run with GFCT (blue), GDCT (green), NoCT (magenta), and mean profiles as simulated in the 1-km cloud-resolved WRF-Chem run (black), compared with the IC for cloud-parameterized run (blue dash) and cloud-resolved run (black dash) based on the model output along the aircraft sampling track. The error bars indicate one standard deviation.

and NoCT) are small, which is because the grid-scale convective transport rather than the subgrid-scale transport dominates in the 12-km runs.

For the 11 June MCS case, all three 36-km runs simulated the CO increase in the UT region (Figures 8c, 8e, and 8g); however, similar to the 29 May supercell case, the simulated outflow regions for all the parameterized convection runs were smaller than the observed anvil region, which might be due to the lack of ice physics simulation in all the cloud schemes used in this paper. The lack of ice physics simulation would affect the simulation of UT buoyance field, such that the vertical and horizontal structure of the upper level cloud was not well simulated. For this case, the aircraft only measured in the edge of the storm anvil region. In order to evaluate the simulation in the storm core region, we compared the cloud-parameterized simulations with the cloud-resolved simulation (Figure 8b). Nevertheless, only the GFCT (Figure 8c) reproduced the large CO mixing ratio ($>$125 ppbv) in the storm core region, which was seen in the cloud-resolved run (Figure 8b). At 12-km resolution (Figures 8d, 8f, and 8h), the CO mixing ratio results from the three cloud-parameterized runs were similar.

In Figure 10a, within the aircraft measuring height range, the observed mean in-cloud CO mixing ratio was 113 ppbv. The GFCT-simulated in-cloud CO mixing ratio was 115 ppbv, and the simulated UT CO mixing ratio from the other two cloud-parameterized runs was smaller than the GFCT results (GDCT: 110 ppbv; NoCT: 107 ppbv). The increase when GFCT was used was not as apparent as the increase in the 29 May supercell case. This result implies that the subgrid convective transport was more significant in the supercell case than in the MCS case. For the result at 12-km resolution (Figure 10b), in the UT, all the simulation results were close to the observation. In the lower troposphere, at both 12- and 36-km resolution, GFCT- and GDCT-simulated CO mixing ratios were smaller than the NoCT result. This result is because in the downdraft region of the MCS, there was injection of relatively clean midlevel clean air to the storm downdraft, which then descended to the lower troposphere and decreased the CO mixing ratio in this region. This result is also found in the cloud-resolved results (Li et al., 2017).

5.3. Comparison of Subgrid Convective Transport and Turbulent Mixing

We also investigated whether vertical turbulent mixing may also affect the convective transport of PBL CO to the upper levels. In order to contrast the influence of vertical turbulent mixing and subgrid convective transport on the CO vertical profile, we conducted four sensitivity runs: (1) GFCT with trace gas turbulent mixing (vertmix_onoff = 1), (2) GFCT without trace gas turbulent mixing (vertmix_onoff = 0), (3) NoCT with trace gas turbulent mixing, and (4) NoCT without trace gas turbulent mixing. Turning vertical turbulent mixing off in this manner did not affect the meteorological simulation. Results showed that the difference between turning on and turning off turbulent mixing was negligible, in the midtroposphere and UT, particularly in the supercell case. In the lower troposphere (under 2 km), the difference between turning on and off vertical mixing was significant but not particularly large (5% for 29 May supercell case and 13% for 11 June MCS case). Without turbulent mixing, the vertical gradient of the low-level CO mixing ratio was larger.

5.4. Comparison of Subgrid-Scale and Grid-Scale Convective Transport

We compared the subgrid- and grid-scale convective transport by analyzing the CO tendency in the convective region due to convective transport. The CO tendency due to subgrid-scale convective transport is calculated using equation (4), and the CO tendency due to grid-scale convective transport is calculated using the following equation:

$$\left(\frac{\partial C}{\partial \mathrm{t}}\right)_{\mathrm{grid}} = \left[\left(\mathrm{advh\_co}_{t+1} + \mathrm{advz\_co}_{t+1}\right) - \left(\mathrm{advh\_co}_{t} + \mathrm{advz\_co}_{t}\right)\right]/\mathrm{dt} \tag{5}$$

where advz_co and advh_co represent the changes in CO concentration due to grid-scale vertical and horizontal advection accumulated in time since the beginning of the simulation. $\left(\frac{\partial C}{\partial t}\right)_{\mathrm{grid}}$ was close to zero in grid boxes not affected by the convection, convection downwind, or emission. Therefore, we call $\left(\frac{\partial C}{\partial t}\right)_{\mathrm{grid}}$ the CO tendency due to grid-scale convective transport. We calculated the CO tendency for two regions: where the simulated precipitation rate was $>$0 mm/hr and where the simulated precipitation rate was $>$3 mm/hr. The $>$0-mm/hr results provide us information on convective transport from the beginning of the storm to the end of the simulation, especially at the start of the storm when the precipitation was not strong. Comparing the

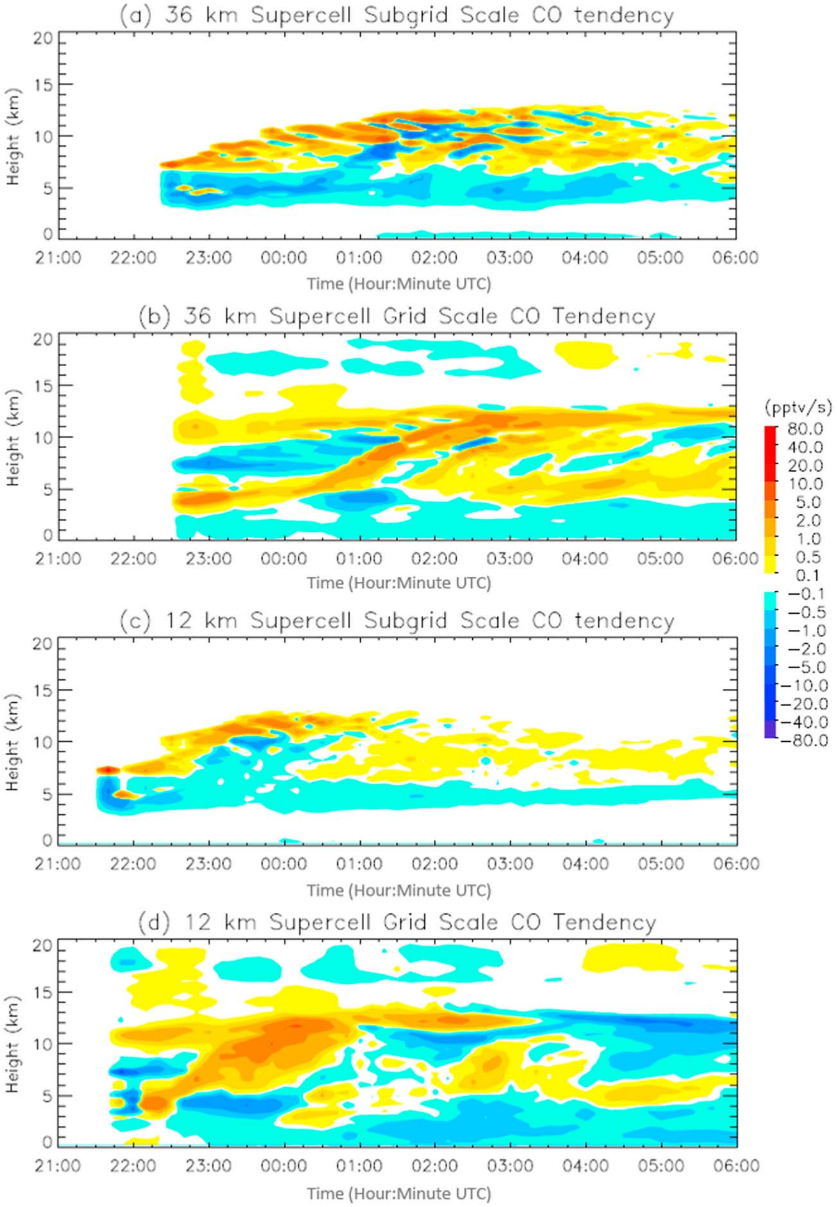

Figure 11. Subgrid-scale CO tendency (pptv/s) averaged over the region where simulated precipitation >0 mm/hr for the 29 May supercell case at (a) 36- and (c) 12-km horizontal resolution domain and grid-scale CO tendency (pptv/s) at (b) 36- and (d) 12-km horizontal resolution domain.

>0-mm/hr results with the >3-mm/hr results enables us to see the relationship between convective transport and the precipitation rate.

The CO tendency results for the 29 May supercell case are shown in Figures 11 (averaged over grid points where the simulated precipitation rate was greater than 0-mm/hr region) and 12 (averaged over grid points where the simulated precipitation rate was greater than 3-mm/hr region). In both Figures 11 and 12, the CO tendency is most positive in a narrow layer that increases in height from ~4 to ~12 km as the storm develops. According to Li et al. (2017), the altitude of this layer coincides with the layer of maximum detrainment. In Figure 11, the subgrid-scale convective transport started earlier than the grid-scale convective transport in both the simulations at 12- and 36-km resolutions. The subgrid-scale convective transport reached its maximum during the hour prior to the formation of the grid-scale constant altitude maximum CO increase (detrainment) layer in the UT at around 0250 UTC in the simulations

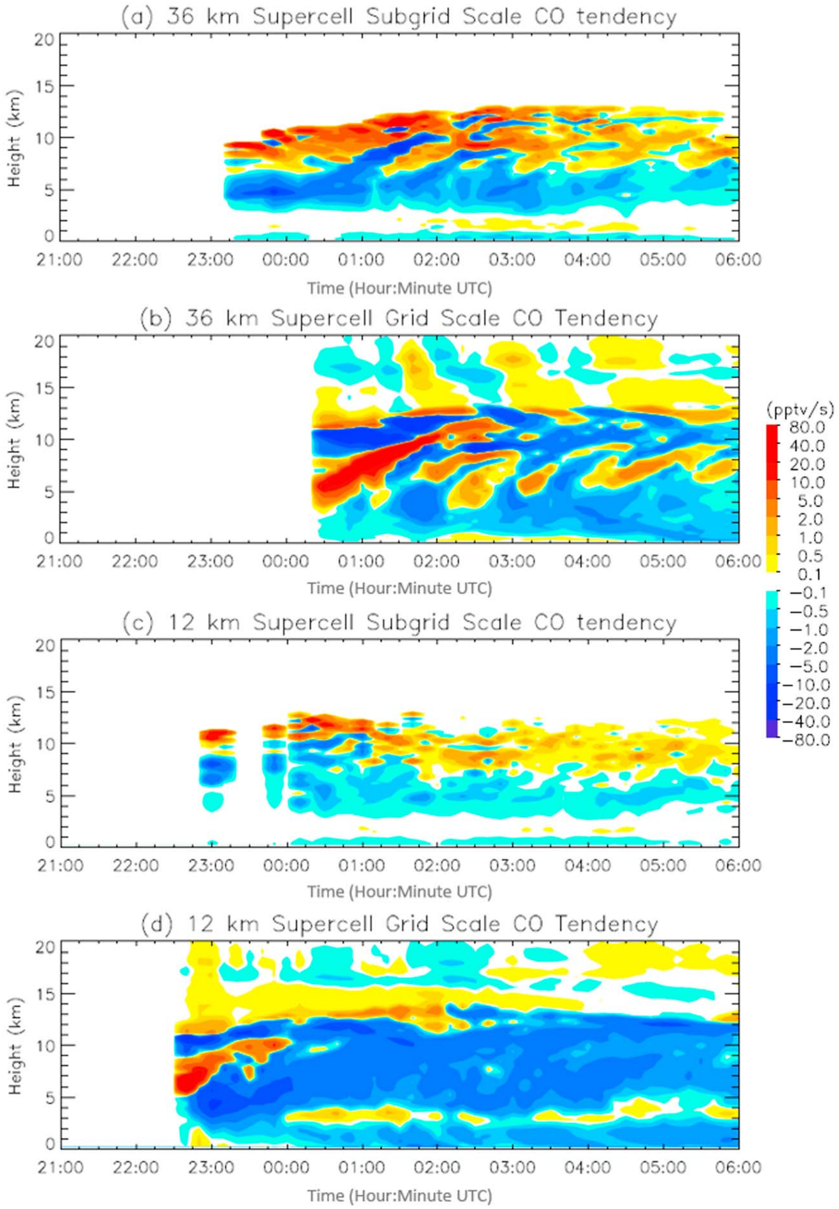

Figure 12. Similar to Figure 11 but for the region where precipitation was greater than 3 mm/hr.

at 36-km resolution and about 0000 UTC in the simulations at 12-km resolution. After that time, the subgrid-scale convective transport began to decay. The grid-scale convective transport of CO at the beginning of the storm was also stronger than when the storm became mature. Comparing Figure 12, with Figure 11, the average grid- and subgrid-scale CO tendencies in the region with the precipitation rate greater than 3 mm/hr were much stronger than the average CO tendency in the >0-mm/hr precipitation rate region, which proves that both grid-scale and subgrid-scale transport are stronger in the heavier precipitation region.

The CO tendency results for the 11 June MCS case are shown in Figures 13 and 14. Compared to the 29 May supercell results, the CO tendencies due to both subgrid- and grid-scale convection in the >0-mm/hr precipitation region were smaller, especially for the 12-km resolution. The magnitude of CO tendency in the stronger precipitation region (>3 mm/hr, Figure 14) was comparable to the 29 May supercell results (Figure 12). Similar to the supercell case, both grid- and subgrid-scale CO tendencies in the MCS case were strongest when the continuous constant-altitude detrainment layer began (1200 UTC). After that time, when the

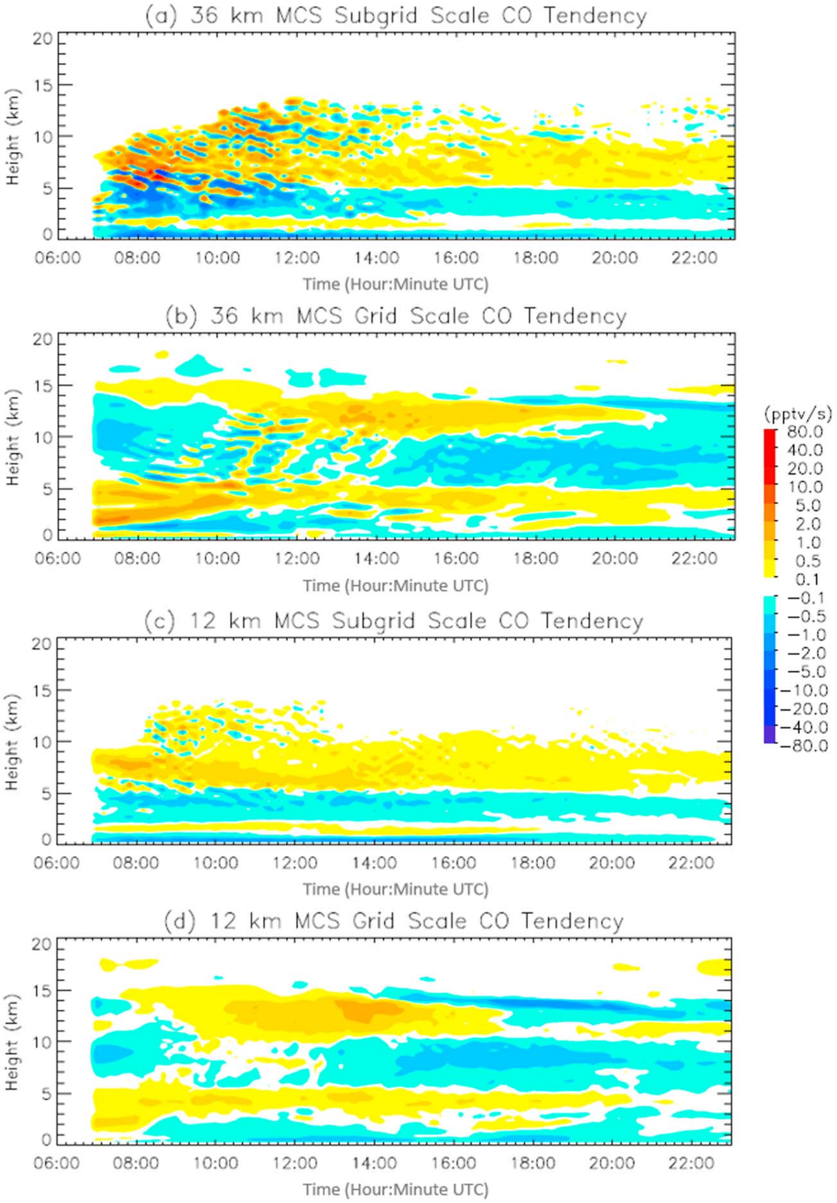

Figure 13. Subgrid-scale CO tendency (pptv/s) for the 11 June MCS case at (a) 36 and (b) 12-km horizontal resolution domain and grid-scale CO tendency (pptv/s) at (b) 36 and (d) 12-km horizontal resolution domain.

storm moved southeastward to the Kentucky and Tennessee region, the mean upper level CO tendency due to grid- and subgrid-scale convection was very weak. Furthermore, unlike the results in the supercell case, the grid-scale transport started at nearly the same time as the subgrid-scale convective transport. This is because in the supercell case, the grid spacing is too coarse to resolve the strength of the convergence at the beginning of the storm. Therefore, the parameterization has to initiate and maintain the convection until the resolved scale can respond to the redistribution of water and heat. While in the MCS case, the convergence occurred over a large enough spatial scale to be resolved in the grid scale at the start of the storm.

In order to further compare the subgrid-scale convective transport with the grid-scale convective transport, we calculate the ratio (R) between the column maximum of horizontally averaged CO increase rate due to subgrid-scale and grid-scale convection at each 10-min interval model output time, and its 1-hr running mean ($\overline{R_{1h}}$), which was plotted in Figure 15, using the following equation:

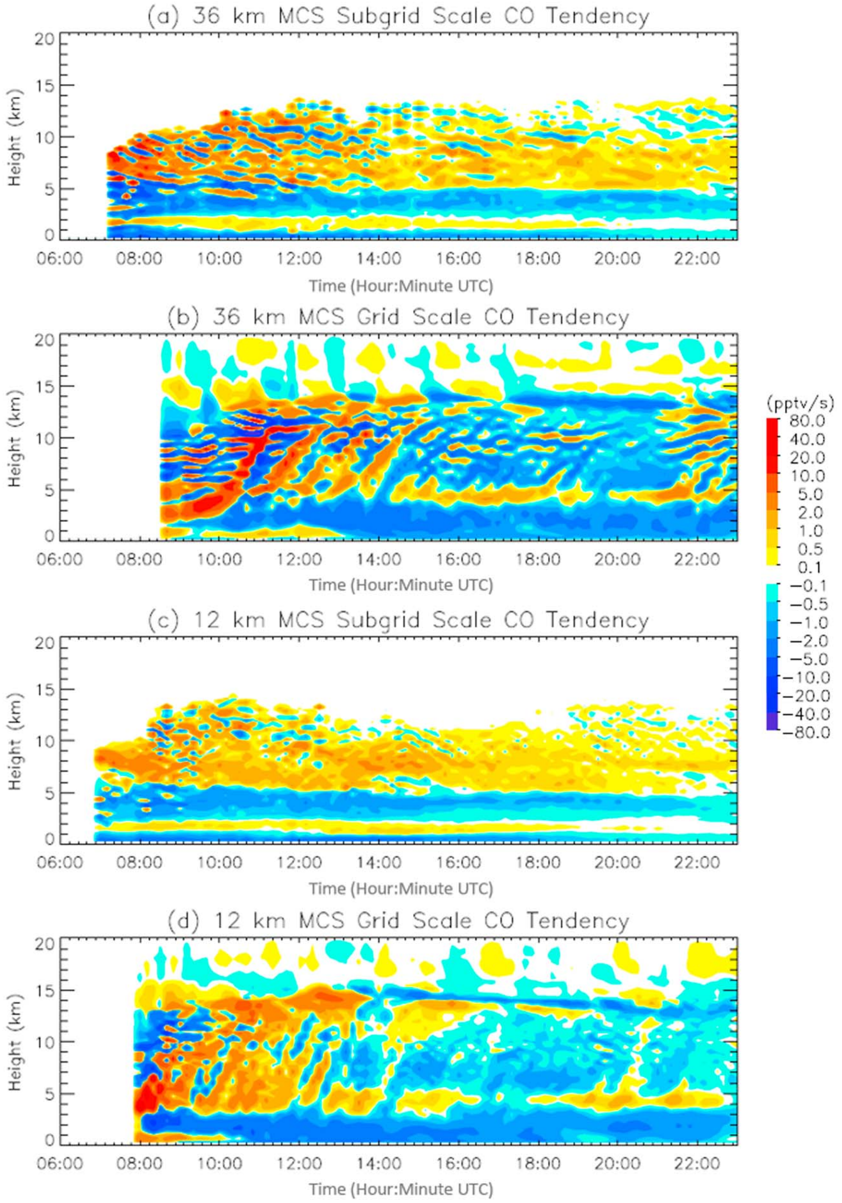

Figure 14. Similar to Figure 13 but for the region where precipitation was greater than 3 mm/hr.

$$R_t = \frac{\max\left(\left(\frac{\overline{\partial C}}{\partial t}\right)_{\text{subgrid }1,t}, \left(\frac{\overline{\partial C}}{\partial t}\right)_{\text{subgrid }2,t}, \left(\frac{\overline{\partial C}}{\partial t}\right)_{\text{subgrid }3,t} \cdots \left(\frac{\overline{\partial C}}{\partial t}\right)_{\text{subgrid}k,t}\right)}{\max\left(\left(\frac{\overline{\partial C}}{\partial t}\right)_{\text{grid }1,t}, \left(\frac{\overline{\partial C}}{\partial t}\right)_{\text{grid }2,t}, \left(\frac{\overline{\partial C}}{\partial t}\right)_{\text{grid }3,t} \cdots \left(\frac{\overline{\partial C}}{\partial t}\right)_{\text{grid}k,t}\right)} \tag{6}$$

$$\overline{R_{1\text{h}}} = \frac{1}{7}\left(\sum_{t=t-3}^{t+3} R_t\right) \tag{7}$$

where t represents the model output time, k represent the model height level, and $\frac{\overline{\partial C}}{\partial t}$ represents the average CO tendency over the points where simulated precipitation was greater than the precipitation threshold at time t and level k. In Figure 15, we show the results before the grid-scale and subgrid-scale CO tendencies began to decay (see Figures 11 and 13). After that time, the grid-scale CO tendency was weak, which led to meaningless large values of the subgrid/grid ratio.

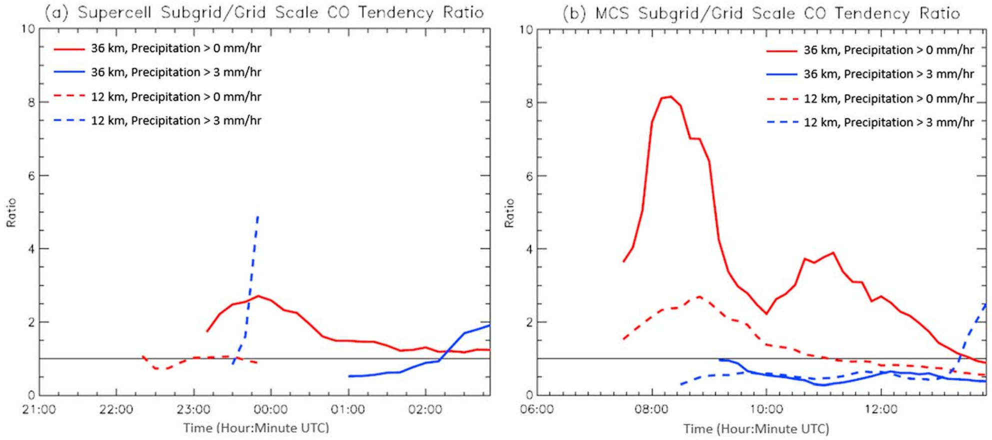

Figure 15. One-hour running means of the subgrid/grid convective transport ratio for the (a) 29 May supercell case and (b) 11 June MCS case.

For the 29 May supercell case (Figure 15), in the simulations at 36-km resolution, the subgrid/grid ratio was smaller in the stronger precipitation region than the precipitation $>$0-mm/hr region. In the $>$0-mm/hr result, the subgrid/grid ratio was always greater than 1 (solid red line), which means that the subgrid-scale convective transport plays a more significant role compared to the grid-scale convective transport. Meanwhile, in the $>$3-mm/hr result, the subgrid/grid ratio (solid blue line) was less than 1, which means that the grid-scale convective transport contributes more. The 36-km results for the MCS case were similar to the 36-km results of the supercell case. In both cases, the subgrid/grid ratios in the simulations at 12-km resolution were smaller than the 36-km results. Thus, the subgrid-scale convection contributes more in the lower resolution domain and when the weaker precipitation region is included (especially in the beginning of the storm). There were some large values in the supercell 12-km precipitation $>$3-mm/hr results, which resulted from the weak grid-scale convective transport at around 0000 UTC.

Wang et al. (1996) found that averaged over the storm duration the subgrid contribution to tracer convective transport was about 48% for a tropical MCS case at 30-km resolution and 64% for a midlatitude squall line case at 25-km resolution. However, as shown in Figure 15, the contribution of subgrid convective transport varies over time, which Wang et al. did not discuss. In this paper, we study the evolution of the subgrid contribution (SC) in the storm region (simulated precipitation $>$0 mm/hr) using the following equation:

$$\mathrm{SC_t} = \frac{\sum_{\mathrm{tstart}}^{\mathrm{t}}\left(\frac{\partial C}{\partial t}\right)_{\mathrm{subgrid}}}{\sum_{\mathrm{tstart}}^{\mathrm{t}}\left(\frac{\partial C}{\partial t}\right)_{\mathrm{subgrid}} + \sum_{\mathrm{tstart}}^{\mathrm{t}}\left(\frac{\partial C}{\partial t}\right)_{\mathrm{grid}}} \tag{8}$$

where *t*start is the earliest time when both subgrid- and grid-scale convection are operating to cause positive CO tendencies at high altitude (8–14 km for the supercell case and 10–16 km for the MCS case). Time series of SC for the first 4 hr (240 min) are shown in Figure 16. Results show that the SC is very large at the beginning

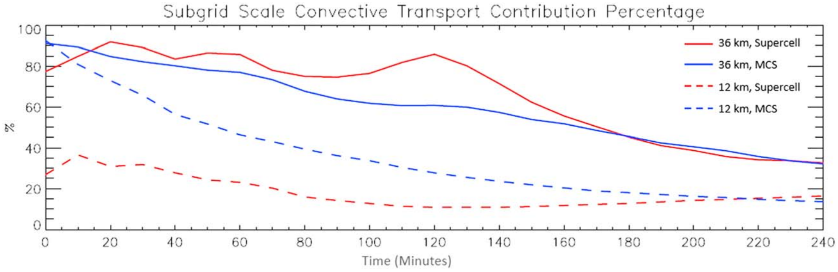

Figure 16. Accumulated subgrid-scale convective transport contribution percentage for 29 May supercell case (red) and 11 June MCS case (blue) at 36- (solid) and 12-km (dash) domain.

but decreases as the storm develops. In the simulations at 36-km resolution, the SC for both cases is initially 90%. After 2 hr, the SC of the supercell case was still over 80%, while the SC of the MCS case was around 65%. After 4 hr, the SC of both cases was around 30%. In the simulations at 12-km resolution, the SC was smaller than the 36-km results. The SC decreased faster in the MCS case than the supercell case, but the SC for the MCS case remained larger than that for the supercell case throughout most of the 4 hr. At 4 hr, the SC for both cases equalled 15%.

6. Conclusions

In this study, we analyze cloud-parameterized deep convective transport for two different convective regimes from the DC3 field campaign using WRF-Chem simulations: a supercell case and an MCS case. The simulations were conducted at horizontal resolutions of 36 and 12 km using one-way nesting. We tried several cumulus parameterization schemes (KF, BMJ, GF, G3, and Tiedke) in WRF with the GF scheme producing the best comparison with observed precipitation. By tuning the closures inside the GF scheme, the model simulation of the precipitation was further improved (maximum precipitation increased by 36%) in the supercell case. The normal GF scheme performed well for the MCS case. The simulation at both resolutions reproduced the storm location and spatial structure. Based on the precipitation, before the aircraft outflow measuring time, the subgrid-scale convection dominated in the simulations at 36-km resolution in both cases, while grid-scale convection dominated in the simulations at 12-km resolution. Based on the precipitation results, our convective transport study was conducted using the GF scheme in the meteorological portion of WRF-Chem.

In order to gain a better simulation of the subgrid convective transport, we replaced the WRF-Chem default scheme for the subgrid convective transport (GDCT) with a scheme that uses the mass fluxes calculated in the GF scheme to calculate the trace gas tendency due to subgrid convective transport (GFCT). Therefore, tracer transport is calculated within the GF scheme in a manner consistent with that done for water vapor. Compared with the results using GDCT and NoCT, the upper level outflow CO mixing ratio for GFCT was 15–18 ppbv (17–18%) larger in the 29 May supercell case resulting in a better agreement with measurements. In the 11 June MCS case, the GFCT improved the upper level CO mixing ratio simulation in the storm core region by ~25 ppbv. Thus, in order to better reproduce the transport of trace gases, subgrid convective transport needs to be consistent with the convective cloud parameterization in the meteorological model that drives the chemical transport, which is not generally the case in current-generation chemical transport models such as WRF-Chem and CMAQ. Furthermore, the CO mixing ratio improvement in the 29 May case was greater than in the 11 June case implying that the subgrid convective transport may be more important in supercells than MCSs. In addition in the MCS case, we found that subgrid-scale transport results in lower CO mixing ratios near the surface due to an injection of relatively clean midlevel air to the storm downdraft, which then descends to the lower troposphere and decreases the CO mixing ratio. The GFCT scheme was able to capture this feature, which is in agreement with a cloud-resolved simulation of the storm.

Although the GFCT scheme improved the upper level outflow CO simulation, the 36-km cloud parameterized CO mixing ratios within the upper tropospheric cloud were still smaller than the aircraft observations and the cloud-resolved CO mixing ratio. In addition, the cloud-parameterized CO in the outflow region on the downwind side was smaller than in the observations and cloud-resolved simulation.

Furthermore, we compared the impact of vertical turbulent mixing with the subgrid convective transport. Results indicated that in the UT, the difference between turning on and turning off turbulent mixing was negligible. The subgrid convective transport dominated the vertical redistribution of the CO. However, in the lower troposphere the turbulent mixing effect was essential to a good simulation.

Moreover, we examined the CO tendency due to subgrid convective transport and grid-scale convective transport. Results showed that the subgrid-scale convective transport started earlier than the grid-scale convective transport in the supercell case. This result is likely because the grid spacing is too coarse to resolve the strength of the convergence at the beginning of the storm. Therefore, the parameterization has to initiate the storm. The cumulus parameterization redistributed water and heat by incrementing the moisture and temperature tendency at the appropriate grid points. After several time steps, the resolved scale responded to the redistribution of the water and heat and grid-scale convection started. In the MCS case, the grid scale resolved the strength of the convergence at the start of the storm. Therefore, the grid-scale transport occurred nearly at the same time with the subgrid-scale convective transport. As the storm started to develop, the CO detrainment layer at the storm top increased in height. The subgrid-scale convective transport reached its maximum during the hour prior to the formation of the grid-scale constant altitude maximum CO increase (detrainment) layer in the UT. After that time, both the subgrid- and grid-scale convective transport began to decay. Both the grid-scale and subgrid-scale CO tendencies in the supercell case were larger than in the MCS case. Furthermore, the subgrid-scale convective transport played a more significant role in the supercell case than the MCS case. By comparing the CO tendency in different precipitation rate regimes, we found that both subgrid- and grid-scale convective transport were stronger in the higher-precipitation region. The analysis of the subgrid/grid ratio demonstrated that during the development of the storm, the subgrid-scale convection contributes more in the lower resolution domain and weak precipitation region (i.e., in the beginning of the storm).

Finally, we examine the subgrid contribution (SC) to the CO transport. Results show that the SC is very large at the beginning but decreases as the storm develops. In the simulations at 36-km resolution, at the beginning the SC for both cases equalled 90%. After 4 hr, the SC decreased to 30% for both cases. In the simulations at 12-km resolution, the SC was smaller than the 36-km results. The SC decreased faster in the MCS case than the supercell case. After 4 hr, the SC for both cases was around 15%.

A major conclusion of this work is that to obtain reasonable simulations of the impact of convection on tropospheric composition, subgrid convective transport needs to be computed in a manner consistent with the subgrid convection in the driving meteorological model. This is true regardless of whether the chemical transport is computed on line with the meteorology or in an offline manner. If cumulus schemes other than GF are used, the convective transport needs to be performed consistently with those schemes.

In this work, we found that the GF scheme underestimates the size of the high-level anvil region (CO outflow region), which might result from the lack of cloud ice physics in the GF scheme. In the future, we suggest to add cloud ice physics in the GF scheme to improve the simulation of cloud anvil and the high-level outflow region of trace gases. Moreover, in this paper, the subgrid convective transport of CO, an insoluble trace gas with a lifetime much longer than the storm duration, was examined. Another gap in our understanding is the convective transport of soluble trace gases, such as HNO_3, CH_2O, CH_3OOH, H_2O_2, and SO_2, where wet deposition plays an important role. These gases are important precursors of ozone and aerosol in the UT. In the future, we will study the subgrid-scale wet scavenging of these precursors and improve the model simulation of deep convective transport of soluble gases through consideration of the retention efficiency of soluble species in ice. Such improvements will help predict the transport of air pollutants and characterize the effect of ozone and aerosol on the Earth radiation budget.

Acknowledgments
This work was supported under NSF grant AGS-1522551 for analysis and modeling associated with the Deep Convective Clouds and Chemistry (DC3) field campaign. M. Bela was supported by NASA ACCDAM-NNX14AR56G and a National Research Council Research Associateship in the Global Systems Division (GSD) at NOAA-ESRL. K. Cummings was also employed by NASA through the NASA Pathways Program during completion of this research. We thank the NCAR Computational Systems Laboratory (CISL) for usage of the Yellowstone supercomputer for conducting the storm simulations. NCAR is operated by the University Corporation for Atmospheric Research under sponsorship of the National Science Foundation. We extend our appreciation to Glen Diskin and Teresa Campos, respectively, for the DC8 and GV observations of CO. We would like to thank C. R. Homeyer who provided us the NEXRAD data. We thank Georg Grell for helpful discussions. The DC3 merged aircraft data are available at http://www-air.larc.nasa.gov/cgibin/ArcView/dc3; NCEP Stage IV precipitation analysis is available at http://www.emc.ncep.noaa.gov/mmb/ylin/pcpanl/stage4/; NAM-ANL is available at http://nomads.ncdc.noaa.gov/data/namanl/; GFS analyses and forecasts are available at https://www.ncdc.noaa.gov/data-access/model-data/model-datasets/global-forcast-system-gfs; MOZART-4 global model output is available at http://www.acom.ucar.edu/wrf-chem/mozart.shtml. We appreciate the discussions with Xin-Zhong Liang and Georg Grell on this work. WRF-Chem model code is available here https://doi.org/10.5281/zenodo.1411968.

References

Apel, E. C., Hornbrook, R. S., Hills, A. J., Blake, N. J., Barth, M. C., Weinheimer, A., et al. (2015). Upper tropospheric ozone production from lightning NO_x-impacted convection: Smoke ingestion case study from the DC3 campaign. *Journal of Geophysical Research: Atmospheres*, *120*, 2523–2505. https://doi.org/10.1002/2014JD022121

Arakawa, A., Jung, J.-H., & Wu, C.-M. (2011). Toward unification of the multiscale modeling of the atmosphere. *Atmospheric Chemistry and Physics*, *11*(8), 3731–3742. https://doi.org/10.5194/acp-11-3731-2011

Arakawa, A., & Schubert, W. H. (1974). Interaction of a cumulus cloud ensemble with the large-scale environment. Part I. *Journal of the Atmospheric Sciences*, *31*(3), 674–701. https://doi.org/10.1175/1520-0469(1974)031<0674:IOACCE>2.0.CO;2

Barth, M. C., Cantrell, C. A., Brune, W. H., Rutledge, S. A., Crawford, J. H., Huntrieser, H., et al. (2015). The Deep Convective Clouds and Chemistry (DC3) field campaign. *Bulletin of the American Meteorological Society*, *96*(8), 1281–1309. https://doi.org/10.1175/BAMS-D-13-00290.1

Barth, M. C., Lee, J., Hodzic, A., Pfister, G., Skamarock, W. C., Worden, J., et al. (2012). Thunderstorms and upper troposphere chemistry during the early stages of the 2006 North American Monsoon. *Atmospheric Chemistry and Physics*, *12*(22), 11,003–11,026. https://doi.org/10.5194/acp-12-11003-2012

Bechtold, P., Semane, N., Lopez, P., Chaboureau, J.-P., Beljaars, A., & Bormann, N. (2014). Representing equilibrium and nonequilibrium convection in large-scale models. *Journal of the Atmospheric Sciences*, *71*(2), 734–753. https://doi.org/10.1175/JAS-D-13-0163.1

Bela, M. M., Barth, M. C., Toon, O. B., Fried, A., Homeyer, C. R., Morrison, H., et al. (2016). Wet scavenging of soluble gases in DC3 deep convective storms using WRF-Chem simulations and aircraft observations. *Journal of Geophysical Research: Atmospheres*, *121*, 4233–4257. https://doi.org/10.1002/2015JD024623

Bela, M. M., Barth, M. C., Toon, O. B., Fried, A., Ziegler, C., Cummings, K. A., et al. (2018). Effects of scavenging, entrainment, and aqueous chemistry on peroxides and formaldehyde in deep convective outflow over the central and Southeast United States. *Journal of Geophysical Research: Atmospheres*, *123*. https://doi.org/10.1029/2018JD028271

Bertram, T. H., Perring, A. E., Wooldridge, P. J., Crounse, J. D., Kwan, A. J., Wennberg, P. O., et al. (2007). Direct measurements of the convective recycling of the upper troposphere. *Science*, *315*(5813), 816–820. https://doi.org/10.1126/science.1134548

Bigelbach, B. C., Mullendore, G. L., & Starzec, M. (2014). Differences in deep convective transport characteristics between quasi-isolated strong convection and mesoscale convective systems using seasonal WRF simulations. *Journal of Geophysical Research: Atmospheres*, *119*, 11,445–11,455. https://doi.org/10.1002/2014JD021875

Brown, J. M. (1979). Mesoscale unsaturated downdrafts driven by rainfall evaporation: A numerical study. *Journal of the Atmospheric Sciences*, *36*(2), 313–338. https://doi.org/10.1175/1520-0469(1979)036<0313:MUDDBR>2.0.CO;2

Chatfield, R. B., & Crutzen, P. J. (1984). Sulfur dioxide in remote oceanic air: Cloud transport of reactive precursors. *Journal of Geophysical Research*, *89*, 7111–7132. https://doi.org/10.1029/JD089iD05p07111

Dickerson, R. R., Huffman, G. J., Luke, W. T., Nunnermacker, L. J., Pickering, K. E., Leslie, A. C. D., et al. (1987). Thunderstorms: An important mechanism in the transport of air pollutants. *Science*, *235*(4787), 460–465. https://doi.org/10.1126/science.235.4787.460

DiGangi, E. A., MacGorman, D. R., Ziegler, C. L., Betten, D., Biggerstaff, M., Bowlan, M., & Potvin, C. K. (2016). An overview of the 29 May 2012 Kingfisher supercell during DC3. *Journal of Geophysical Research: Atmospheres*, *121*, 14,316–14,343. https://doi.org/10.1002/2016JD025690

Fast, J. D., Gustafson, W. I., Easter, R. C., Zaveri, R. A., Barnard, J. C., Chapman, E. G., et al. (2006). Evolution of ozone, particulates, and aerosol direct radiative forcing in the vicinity of Houston using a fully coupled meteorology-chemistry-aerosol model. *Journal of Geophysical Research*, *111*, D21305. https://doi.org/10.1029/2005JD006721

Frank, W. M., & Cohen, C. (1987). Simulation of tropical convective systems. Part I: A cumulus parameterization. *Journal of the Atmospheric Sciences*, *44*(24), 3787–3799. https://doi.org/10.1175/1520-0469(1987)044<3787:SOTCSP>2.0.CO;2

Freitas, S., Dias, M., & Silva Dias, P. (2000). Modeling the convective transport of trace gases by deep and moist convection. *Hybrid Methods in Engineering*, *2*, 315–328.

Fried, A., Barth, M. C., Bela, M., Weibring, P., Richter, D., Walega, J., et al. (2016). Convective transport of formaldehyde to the upper troposphere and lower stratosphere and associated scavenging in thunderstorms over the central United States during the 2012 DC3 study. *Journal of Geophysical Research: Atmospheres*, *121*, 7430–7460. https://doi.org/10.1002/2015JD024477

Grell, G. A. (1993). Prognostic evaluation of assumptions used by cumulus parameterizations. *Monthly Weather Review*, *121*(3), 764–787. https://doi.org/10.1175/1520-0493(1993)121<0764:PEOAUB>2.0.CO;2

Grell, G. A., & Devenyi, D. (2002). A generalized approach to parameterizing convection combining ensemble and data assimilation techniques. *Geophysical Research Letters*, *29*(14), 1693. https://doi.org/10.1029/2002GL015311

Grell, G. A., Dudhia, J., & Stauffer, D. R. (1994). A description of the Fifth Generation Penn State/NCAR Mesoscale Model (MM5), NCAR Tech Note TN-398 + STR (122 pp.).

Grell, G. A., & Freitas, S. R. (2014). A scale and aerosol aware stochastic convective parameterization for weather and air quality modeling. *Atmospheric Chemistry and Physics*, *14*(10), 5233–5250. https://doi.org/10.5194/acp-14-5233-2014

Grell, G. A., Peckham, S. E., Schmitz, R., McKeen, S. A., Frost, G., Skamarock, W. C., & Eder, B. (2005). Fully coupled "online" chemistry within the WRF model. *Atmospheric Environment*, *39*(37), 6957–6975. https://doi.org/10.1016/j.atmosenv.2005.04.027

Halland, J. J., Fuelberg, H. E., Pickering, K. E., & Luo, M. (2009). Identifying convective transport of carbon monoxide by comparing remotely sensed observations from TES with cloud modeling simulations. *Atmospheric Chemistry and Physics*, *9*(13), 4279–4294. https://doi.org/10.5194/acp-9-4279-2009

Homeyer, C. R., Pan, L. L., Dorsi, S. W., Avallone, L. M., Weinheimer, A. J., O'Brien, A. S., et al. (2014). Convective transport of water vapor into the lower stratosphere observed during double-tropopause events. *Journal of Geophysical Research: Atmospheres*, *119*, 10,941–10,958. https://doi.org/10.1002/2014JD021485

Hong, S.-Y., Noh, Y., & Dudhia, J. (2006). A new vertical diffusion package with an explicit treatment of entrainment processes. *Monthly Weather Review*, *134*(9), 2318–2341. https://doi.org/10.1175/MWR3199.1

Iacono, M. J., Delamere, J. S., Mlawer, E. J., Shephard, M. W., Clough, S. A., & Collins, W. D. (2008). Radiative forcing by long-lived greenhouse gases: Calculations with the AER radiative transfer models. *Journal of Geophysical Research*, *113*, D13103. https://doi.org/10.1029/2008JD009944

Janjić, Z. I. (1994). The Step-Mountain Eta Coordinate Model: Further developments of the convection, viscous sublayer, and turbulence closure schemes. *Monthly Weather Review*, *122*(5), 927–945. https://doi.org/10.1175/1520-0493(1994)122<0927:TSMECM>2.0.CO;2

Janjić, Z. I. (2000). Comments on "Development and Evaluation of a Convection Scheme for Use in Climate Models." *Journal of Atmospheric Science*, *57*, 3686–3686.

Jensen, E. J., Pfister, L., Ueyama, R., Bergman, J. W., & Kinnison, D. (2015). Investigation of the transport processes controlling the geographic distribution of carbon monoxide at the tropical tropopause. *Journal of Geophysical Research: Atmospheres*, *120*, 2086–2067. https://doi.org/10.1002/2014JD022661

Jung, E., Shao, Y., & Sakai, T. (2005). A study on the effects of convective transport on regional-scale Asian dust storms in 2002. *Journal of Geophysical Research*, *110*, D20201. https://doi.org/10.1029/2005JD005

Kain, J. S. (2004). The Kain–Fritsch convective parameterization: An update. *Journal of Applied Meteorology*, *43*(1), 170–181. https://doi.org/10.1175/1520-0450(2004)043<0170:TKCPAU>2.0.CO;2

Kain, J. S., & Fritsch, J. M. (1993). Convective parameterization for mesoscale models: The Kain-Fritsch scheme. In K. A. Emanuel & D. J. Raymond (Eds.), *The representation of cumulus convection in numerical models*, *Meteorological monographs* (Chap. 16, pp. 165–170). Boston, MA: American Meteorological Society. https://doi.org/10.1007/978-1-935704-13-3_16

Kong, F., & Qin, Y. (1993). The vertical transport of air pollutants by convective clouds. Part I: A non-reactive cloud transport model. *Advances in Atmospheric Sciences*, *10*, 415–427.

Kong, F., & Qin, Y. (1994a). The vertical transport of air pollutants by convective clouds. Part II: Transport of soluble gases and sensitivity tests. *Advances in Atmospheric Sciences*, *11*, 1–12.

Kong, F., & Qin, Y. (1994b). The vertical transport of air pollutants by convective clouds. Part III: Transport features of different cloud systems. *Advances in Atmospheric Sciences*, *11*, 13–26.

Koren, V., Schaake, J., Mitchell, K., Duan, Q.-Y., Chen, F., & Baker, J. M. (1999). A parameterization of snowpack and frozen ground intended for NCEP weather and climate models. *Journal of Geophysical Research*, *104*, 19,569–19,585. https://doi.org/10.1029/1999JD900232

Krishnamurti, T. N., Low-Nam, S., & Pasch, R. (1983). Cumulus parameterization and rainfall rates: II. *Monthly Weather Review*, *111*(4), 815–828. https://doi.org/10.1175/1520-0493(1983)111<0815:CPARRI>2.0.CO;2

Levizzani, V., & Setvák, M. (1996). Multispectral, high-resolution satellite observations of plumes on top of convective storms. *Journal of the Atmospheric Sciences*, *53*(3), 361–369. https://doi.org/10.1175/1520-0469(1996)053<0361:MHRSOO>2.0.CO;2

Li, Y. (2018). WRF-Chem code with update of subgrid convective transport of trace gases. https://doi.org/10.5281/zenodo.1411968

Li, Y., Pickering, K. E., Allen, D. J., Barth, M. C., Bela, M. M., Cummings, K. A., et al. (2017). Evaluation of deep convective transport in storms from different convective regimes during the DC3 field campaign using WRF-Chem with lightning data assimilation. *Journal of Geophysical Research:Atmospheres*, *122*, 7140–7163. https://doi.org/10.1002/2017JD026461

Livesey, N. J., Logan, J. A., Santee, M. L., Waters, J. W., Doherty, R. M., Read, W. G., et al. (2013). Interrelated variations of O_3, CO and deep convection in the tropical/subtropical upper troposphere observed by the Aura Microwave Limb Sounder (MLS) during 2004–2011. *Atmospheric Chemistry and Physics*, *13*(2), 579–598. https://doi.org/10.5194/acp-13-579-2013

Lyons, W. A., Calby, R. H., & Keen, C. S. (1986). The impact of mesoscale convective systems on regional visibility and oxidant distributions during persistent elevated pollution episodes. *Journal of Climate and Applied Meteorology*, *25*(11), 1518–1531. https://doi.org/10.1175/1520-0450(1986)025<1518:TIOMCS>2.0.CO;2

Morrison, H., Thompson, G., & Tatarskii, V. (2009). Impact of cloud microphysics on the development of trailing Stratiform precipitation in a simulated squall line: Comparison of one- and two-moment schemes. *Monthly Weather Review*, *137*(3), 991–1007. https://doi.org/10.1175/2008MWR2556.1

Mullendore, G. L., Durran, D. R., & Holton, J. R. (2005). Cross-tropopause tracer transport in midlatitude convection. *Journal of Geophysical Research*, *110*, D06113. https://doi.org/10.1029/2004JD005059

Ott, L. E., Bacmeister, J., Pawson, S., Pickering, K., Stenchikov, G., Suarez, M., et al. (2009). Analysis of convective transport and parameter sensitivity in a single column version of the Goddard Earth Observation System, version 5, general circulation model. *Journal of the Atmospheric Sciences*, *66*(3), 627–646. https://doi.org/10.1175/2008JAS2694.1

Peckham, S., Grell, G. A., McKeen, S. A., Barth, M., Pfister, G., Wiedinmyer, C., et al. (2011). WRF-Chem Version 3.3 User's Guide. NOAA Technical Memo, 98.

Phoenix, D. B., Homeyer, C. R., & Barth, M. C. (2017). Sensitivity of simulated convection-driven stratosphere-troposphere exchange in WRF-Chem to the choice of physical and chemical parameterization. *Earth and Space Science*, *4*(8), 454–471. https://doi.org/10.1002/2017EA000287

Pickering, K. E., Dickerson, R. R., Huffman, G. J., Boatman, J. F., & Schanot, A. (1988). Trace gas transport in the vicinity of frontal convective clouds. *Journal of Geophysical Research*, *93*, 759–773. https://doi.org/10.1029/JD093iD01p00759

Pickering, K. E., Scala, J. R., Thompson, A. M., Tao, W.-K., & Simpson, J. (1992). A regional estimate of convective transport of CO from biomass burning. *Geophysical Research Letters*, *19*, 289–292. https://doi.org/10.1029/92GL00036

Pickering, K. E., Thompson, A. M., Dickerson, R. R., Luke, W. T., McNamara, D. P., Greenberg, J. P., & Zimmerman, P. R. (1990). Model calculations of tropospheric ozone production potential following observed convective events. *Journal of Geophysical Research*, *95*, 14,049–14,062. https://doi.org/10.1029/JD095iD09p14049

Pickering, K. E., Thompson, A. M., Kim, H., DeCaria, A. J., Pfister, L., Kucsera, T. L., et al. (2001). Trace gas transport and scavenging in PEM-Tropics B South Pacific Convergence Zone convection. *Journal of Geophysical Research*, *106*, 32,591–32,607. https://doi.org/10.1029/2001JD000328

Pickering, K. E., Thompson, A. M., Scala, J. R., Tao, W.-K., Dickerson, R. R., & Simpson, J. (1992). Free tropospheric ozone production following entrainment of urban plumes into deep convection. *Journal of Geophysical Research*, *97*, 17,985–18,000. https://doi.org/10.1029/92JD01716

Pickering, K. E., Thompson, A. M., Scala, J. R., Tao, W.-K., & Simpson, J. (1992). Ozone production potential following convective redistribution of biomass burning emissions. *Journal of Atmospheric Chemistry*, *14*, 297–313.

Pickering, K. E., Thompson, A. M., Wang, Y., Tao, W.-K., McNamara, D. P., Kirchhoff, V. W. J. H., et al. (1996). Convective transport of biomass burning emissions over Brazil during TRACE A. *Journal of Geophysical Research*, *101*, 23,993–24,012. https://doi.org/10.1029/96JD00346

Qiao, F., & Liang, X.-Z. (2015). Effects of cumulus parameterizations on predictions of summer flood in the Central United States. *Climate Dynamics*, *45*(3-4), 727–744. https://doi.org/10.1007/s00382-014-2301-7

Qiao, F., & Liang, X.-Z. (2016). Effects of cumulus parameterization closures on simulations of summer precipitation over the United States coastal oceans. *Journal of Advances in Modeling Earth Systems*, *8*(2), 764–785. https://doi.org/10.1002/2015MS000621

Qiao, F., & Liang, X.-Z. (2017). Effects of cumulus parameterization closures on simulations of summer precipitation over the continental United States. *Climate Dynamics*, *49*(1-2), 225–247. https://doi.org/10.1007/s00382-016-3338-6

Scala, J. R., Garstang, M., Tao, W.-K., Pickering, K. E., Thompson, A. M., Simpson, J., et al. (1990). Cloud draft structure and trace gas transport. *Journal of Geophysical Research*, *95*, 17,015–17,030. https://doi.org/10.1029/JD095iD10p17015

Setvák, M., & Doswell, C. A. (1991). The AVHRR Channel 3 Cloud Top Reflectivity of Convective Storms. *Monthly Weather Review*, *119*, 841–847.

Skamarock, W. C., & Klemp, J. B. (2008). A time-split nonhydrostatic atmospheric model for Weather Research And Forecasting applications. *Journal of Computational Physics*, *227*(7), 3465–3485. https://doi.org/10.1016/j.jcp.2007.01.037

Skamarock, W. C., Klemp, J. B., Dudhia, J., Gill, D. O., Barker, D. M., Duda, M. G., et al. (2008). A description of the advanced research WRF version 3. NCAR Technical Note NCAR/TN-475+STR. https://doi.org/10.5065/D68S4MVH

Skamarock, W. C., Powers, J. G., Barth, M., Dye, J. E., Matejka, T., Bartels, D., et al. (2000). Numerical simulations of the July 10 stratospheric-tropospheric experiment: Radiation, aerosols, and ozone/deep convection experiment convective system—Kinematics and transport. *Journal of Geophysical Research*, *105*, 19,973–19,990. https://doi.org/10.1029/2000JD900179

Solomon, S., Rosenlof, K. H., Portmann, R. W., Daniel, J. S., Davis, S. M., Sanford, T. J., & Plattner, G.-K. (2010). Contributions of stratospheric water vapor to decadal changes in the rate of global warming. *Science*, *327*(5970), 1219–1223. https://doi.org/10.1126/science.1182488

Stenchikov, G., Dickerson, R., Pickering, K., Ellis, W., Doddridge, B., Kondragunta, S., et al. (1996). Stratosphere-troposphere exchange in a midlatitude mesoscale convective complex: 2. Numerical simulations. *Journal of Geophysical Research*, *101*, 6837–6851. https://doi.org/10.1029/95JD02468

Thompson, A. M., Pickering, K. E., Dickerson, R. R., Ellis, W. G., Jacob, D. J., Scala, J. R., et al. (1994). Convective transport over the central United States and its role in regional CO and ozone budgets. *Journal of Geophysical Research*, *99*, 18,703–18,711. https://doi.org/10.1029/94JD01244

Tiedtke, M. (1989). A comprehensive mass flux scheme for cumulus parameterization in large-scale models. *Monthly Weather Review*, *117*(8), 1779–1800. https://doi.org/10.1175/1520-0493(1989)117<1779:ACMFSF>2.0.CO;2

Wang, Y., Tao, W.-K., Pickering, K. E., Thompson, A. M., Kain, J. S., Adler, R. F., et al. (1996). Mesoscale model simulations of TRACE A and preliminary regional experiment for storm-scale operational and research meteorology convective systems and associated tracer transport. *Journal of Geophysical Research*, *101*, 24,013–24,027. https://doi.org/10.1029/96JD00933

Yang, Q., Easter, R. C., Campuzano-Jost, P., Jimenez, J. L., Fast, J. D., Ghan, S. J., et al. (2015). Aerosol transport and wet scavenging in deep convective clouds: A case study and model evaluation using a multiple passive tracer analysis approach. *Journal of Geophysical Research: Atmospheres*, *120*, 8448–8468. https://doi.org/10.1002/2015JD023647

Zhang, C., Wang, Y., & Hamilton, K. (2011). Improved representation of boundary layer clouds over the Southeast Pacific in ARW-WRF using a modified Tiedtke cumulus parameterization scheme. *Monthly Weather Review*, *139*(11), 3489–3513. https://doi.org/10.1175/MWR-D-10-05091.1